CHAPTER 2

The Holistic Strategy in Multi-Scale Modeling

Pil Seung Chung[1], **Myung S. Jhon**[1,2] and **Lorenz T. Biegler**[1]

Contents

[1]Department of Chemical Engineering, Carnegie Mellon University, Pittsburgh, PA 15213, USA

[2]School of Advanced Materials Science and Engineering, Sungkyunkwan University, Suwon 440-746, Korea

Advances in Chemical Engineering, Volume 40
ISSN 0065-2377, DOI 10.1016/B978-0-12-380985-8.00002-6

Abstract Theoretical tools for nanoscale systems have become highly advanced over the past decades. Consequently, the demand for novel methodologies, which enable scale-correlated analysis, increases in order to describe a hierarchy of multi-scale systems in various length and time scales. Recent development in the multi-scale approach is becoming popular as a new multidisciplinary analysis paradigm in science and engineering fields. Via hierarchical integration methodologies of various numerical techniques, we can expect a mechanism of communication between different scale phenomena, and predict macroscopic level behavior as functions of other lower level scale parameters. In addition, multi-scale approach can provide integrated system models for decision-making with high accuracy based on first-principle phenomena. In this paper, we present an overview of theoretical tools for specific scales as well as holistic strategies for multi-scale integration by using two benchmark examples: special topics dealing with renewable energy and nanotribology, that is, polymer electrolyte fuel cells and hard disk drive systems.

1. INTRODUCTION

As the demand for nanoscale investigation of systematically specified functional materials increases, novel analytical techniques have been broadly studied to satisfy this demand by tuning physical structures and functionalities of these materials. This progress enlightens the understanding of nanoscale dynamics to control the functionalities of materials. However, advances in nanoanalysis direct us to the critical issue of the interrelation to macroscopic scales since most systems comprise phenomena at different time and length scales, and often can be described through a hierarchy of scale-specific models. Therefore, the multi-scale approach becomes popular as a new multidisciplinary analysis paradigm in science and engineering fields. Via multi-scale approach, we expect that the mechanism of information communication obtained from one scale and passed to another scale, allows one to predict macroscopic behavior from first-principles information in a bottom-up approach. Alternately, device-scale properties can be obtained with nanoscale resolution using the top-down approach. The ultimate goal is to integrate models seamlessly at the

different scales. As system size approaches nanoscale, the observation of phenomena at atomic/molecular scales must be emphasized. In addition, many of the novel approaches to analyze these phenomena have adopted an understanding of the relationship between different scale phenomena, including nanoscopic details where the phenomena cannot be explained by the experiments or macroscopic models (Bent *et al*., 2003; Brown *et al*., 2009; Gerde and Marder, 2001; Juan *et al*., 2009; Moseler *et al*., 2005; Rubla *et al*., 2000).

The vision of the theoretical engineering and science field is currently in multi-scale modeling by coupling computational tools from ab initio atomistic/electronic scales to continuum scale including process and device-level simulation and decision making, and optimizing across different scales. This leads to reversal of the normal flow of knowledge across these scales, and to allow design and synthesis of new forms of matter with tailored properties, driven by large-scale process requirements (Figure 1). Concepts of multi-scale simulation enable us to control the macroscopic phenomena by characterizing nanoscale properties of matter emerging from the complex correlations of atomic constituents. Models based on physics suitable for particular time and length scales use specific numerical techniques to solve the governing equations and answer questions relevant to those scales, which cover the atomistic, molecular, device, and plant levels. To more fully couple advances in knowledge across the enormous range of scales, and enable better understanding and control of emergent properties of matter that emerge from complex interactions, it is necessary to develop holistic multi-scale models, which ensure that knowledge generated at one scale is transmitted to the other. Figure 2 (Grossmann and Westerberg, 2000; Marquardt *et al*, 2000) illustrates multi-scale models and tasks that arise in all applications of process systems engineering.

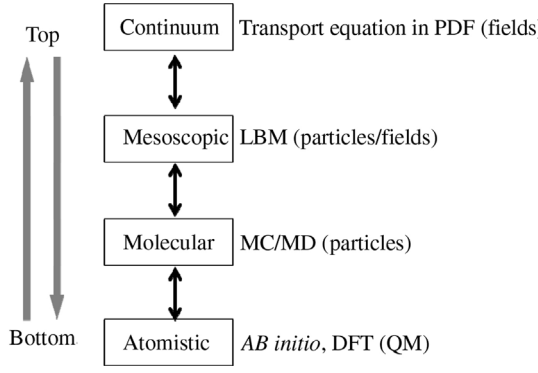

Figure 1 Schematic description of multi-scale approach and modeling methods.

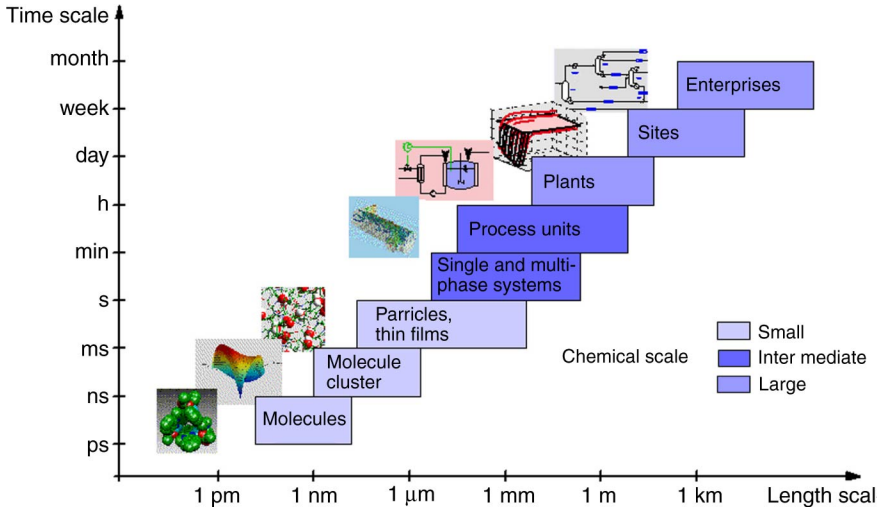

Figure 2 Time and length scales in multi-scale systems engineering.

Both time and length scales cover over 15 orders of magnitude and reflect the behavior of electronic/atomistic/molecular/supramolecular levels all the way to products, process units, and their integration into the enterprise. Moreover, these tasks are strongly intertwined; basic components at the lower scales serve as the building blocks for the scales above them, while the demands at higher scales impose specifications at smaller levels, particularly with respect to material properties. Linkage of submodels ranging from atomistic to the enterprise requires systematic multi-scale, multiphenomena integration, which is the core driver for the current multi-scale modeling paradigm.

During the past 5 years, over 1000 publications have dealt with multi-scale subject and resulting in a broad knowledge of integration methodologies. Some publications provided perspectives on the multi-scale approaches by presenting decision-making methodologies on the applications (Baeurle, 2009; Dudukovic, 2009; Engler *et al.*, 2009; Vlachos, 2005). Among the various multi-scale approaches, which have been developed, we motivate the specific need for multi-scale modeling by focusing on methodologies for the systematic approach to these techniques. In this review paper, we present the holistic integration strategy in multi-scale modeling with two different benchmark applications: special topics dealing with renewable energy and nanotribology, that is, polymer electrolyte fuel cells (PEFC) and hard disk drive (HDD) systems.

2. ILLUSTRATION VIA BENCHMARK EXAMPLES

Owing to the complexity involved in multiphenomena at different time and length scales, the current trends in renewable energy and nanotribology can be excellent benchmark candidates for evaluation of multi-scale modeling approaches. To help understanding of hierarchical systems (Figure 2) of benchmark systems, we will examine PEFC (renewable energy) and HDD system (nanotribology).

2.1 Renewable energy (PEFC)

As the need for renewable energy systems increase, fuel cells have attracted considerable recent attention as a possible replacement for the massive power generation and portable systems. PEFC is one of the promising alternative energy sources for portable or small unit devices (i.e., small scale power generators, and transportations). Since the PEFC consists of nanoscale subsystems including multiphenomena, an accurate system model is needed to design PEFC with optimal performance. Therefore, a fundamental understanding in electrochemistry, materials, and heat and mass transport phenomena are critical for developing accurate models, which can satisfy the high performance and reliability for the fuel cells. The hydrogen PEFC, which directly convert chemical energy into electric energy, is promising candidate for future green car technology in parallel with plug-in and hybrid electric vehicles.

The hydrogen PEFC device comprises a hydrogen source and a gas compressor supplying air in a stack, which consists of multiple PEFCs connected in series (Figure 3) (Xu *et al*., 2006a). An individual PEFC (Figure 4) comprises two gas channels (GCs), two gas diffusion layers (GDLs), and two catalyst layers (CLs) each on the anode and cathode sides, as well as a central polymer electrolyte membrane (PEM). The GCs are bipolar plates that are hollow chambers for fluid inlet and outlet. They also serve as a connection between adjacent cells. The GDLs are porous materials that support the CL, provide uniform distribution of gases, and act as a medium for electron transport from the CL (where the electrochemical reactions typically occur with a platinum (Pt) catalyst) to the external current collectors. The PEM acts as a proton transport passage from anode to the cathode, and this conductivity of the PEM is a strong function of its water uptake. Humidified hydrogen and air are fed to the anode and cathode inlets, respectively. The species undergo transport processes in both the GCs and the porous GDLs, after which they reach the anode/cathode CLs. Within the CLs, hydrogen and oxygen undergo electrochemical reactions, and the water molecules are transported across the PEM from anode to the cathode. The

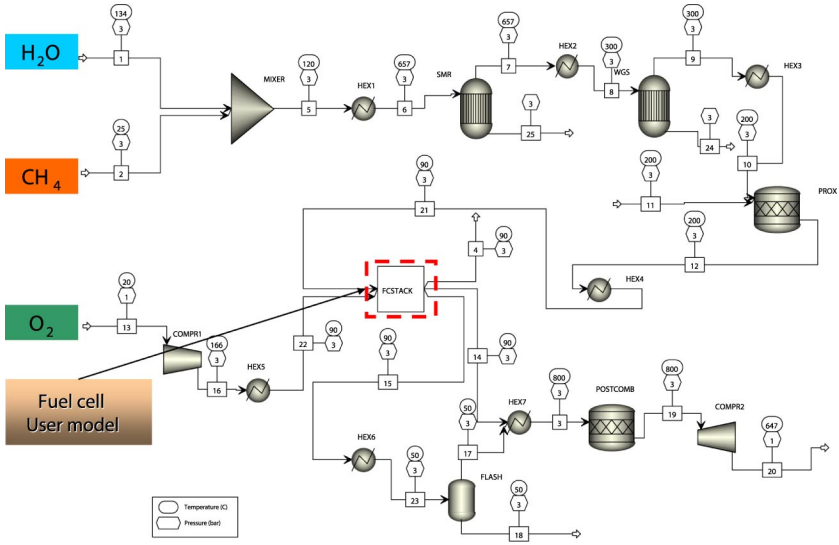

Figure 3 Process-level model of a PEFC-based power plant.

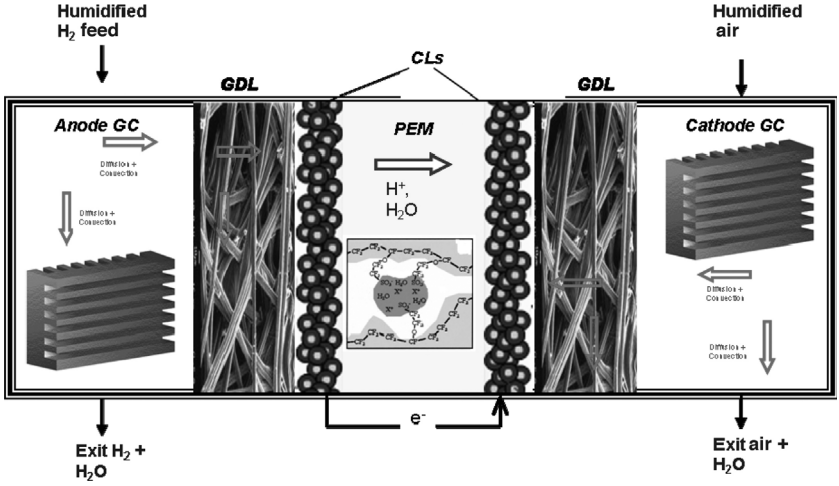

Figure 4 Components of a single stack hydrogen PEFC.

protons released in the oxidation reaction at the anode are transported across the PEM, and electrons released reach the cathode via an external circuit. On reaching the cathode the protons and electrons combine with the oxygen in the reduction reaction to generate water as the product. The direct methanol fuel cell (DMFC) is another type of PEFC, which

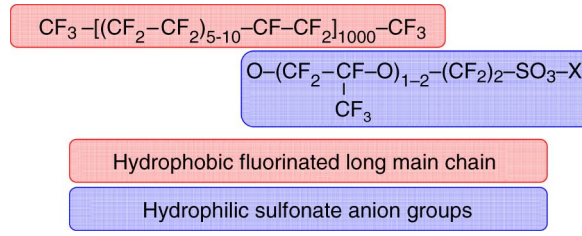

Figure 5 Chemical structure of Nafion®.

uses a solution of methanol and water as a fuel instead of humidified hydrogen gas. Compared to hydrogen fuel cells, DMFCs are advantageous for their ease of fuel delivery and storage, lack of humidification requirement, and reduced design complexity. Due to the absence of ancillary equipments (i.e., fuel reformer), the DMFC is ideally suited for portable electronic devices applicable to laptops or mobile phones (Mench *et al*., 2004).

A PEM is a semipermeable membrane generally made from ionomers and designed to conduct protons while being impermeable to gases such as oxygen or hydrogen. This is their essential function when incorporated into a PEM fuel cell: separation of reactants and transport of protons. One of the most commonly and commercially available PEM materials is Nafion® (Figure 5), which is produced by DuPont. While Nafion® is an ionomer with a perfluorinated backbone like Teflon, there are many other structural motifs used to make ionomers for PEMs. Many use polyaromatic polymers while others use partially fluorinated polymers. Nafion® has received a considerable amount of attention as a proton conductor for PEM fuel cells because of its excellent thermal and mechanical stability. The chemical basis of Nafion®'s superior conductive properties remains a focus of research. Recent reports suggest protons on the $SO_3^-H^+$ (sulfonic acid) groups hop from one acid site to another. The membrane structure allows movement of cations but the membranes do not conduct anions or electrons. Nafion® can be manufactured with various cationic conductivities. In order to operate the membrane must conduct hydrogen ions (protons), but not electrons as this would in effect ''short circuit'' of the fuel cell. The membrane must also not allow gas to pass to the other side of the cell, a problem known as fuel crossover (Baxter *et al*., 1999; Dohle *et al*., 2000; Ren *et al*., 2000), and must be resistant to the reducing environment at the anode as well as the harsh oxidative environment at the cathode. Although the PEFC is a prime candidate of the alternative energy source for the small-scale applications, water management is crucial to performance, as power output requires optimized water uptake in the

membrane. Water management is a very difficult subject in PEM systems. A wide variety of solutions for managing water exist including integration of electro-osmotic pumps. Furthermore, the Pt catalyst on the membrane is easily poisoned by carbon monoxide (no more than one part per million is usually acceptable) and the membrane is sensitive to materials like metal ions, which can be introduced by corrosion of metallic bipolar plates. The commercial viability of this device is hampered currently due to its high cost, power density, and low durability.

Key issues or objectives that are needed to be achieved to make a paradigm shift in PEFC technology are (i) novel materials, obtained through computational chemistry calculations, including PEMs (possessing high-temperature operability and low cost), and electrocatalysts for high reduction reaction kinetics, tolerant to carbon monooxide. Advanced materials need to be discovered for increased durability (with an order of magnitude higher than current technology) and meeting the requirements of environment, safety and health; (ii) optimal design parameters for GDLs (porosity and hydrophobicity), CLs (thickness, composition, and particle size distribution) as well as determination of operating and design conditions (i.e., optimal temperature, pressure, current density, humidity, geometric parameters, flow characteristics and arrangements, etc.). This entire PEFC design can be envisioned as an ultralarge integration of submodels and an optimization problem with the objective function as a combination of maximizing the performance, and minimizing the cost, while maintaining durability. As a series of hierarchical governing equations containing a large set of parameters to be optimized and conditions to be satisfied, multi-scale, multiphenomena models are bound to play a pivotal role in achieving the design goals, in concert with experimentation.

2.2 Nanotribology (HDDs)

Tribology, the subject dealing with friction, wear, and lubrication, becomes important in academic and industrial community. The improved technology on friction and wear would save developed countries up to 1.6% of their gross national product. Such technological considerations have driven humans to understand friction since prehistoric ages. By 200,000 B.C., Neanderthals had achieved a clear mastery of friction, generating fire by the rubbing of wood on wood and by the striking of flint stones. Significant developments are also found 5000 years ago in Egypt, where the transportation of large stone statues for the construction of the pyramids demanded tribological advances in the form of lubricated wooden sledges (Figure 6a). Modern microscopic tribology began 500 years ago, when Leonardo da Vinci deduced the laws governing the motion of a rectangular block sliding over a flat

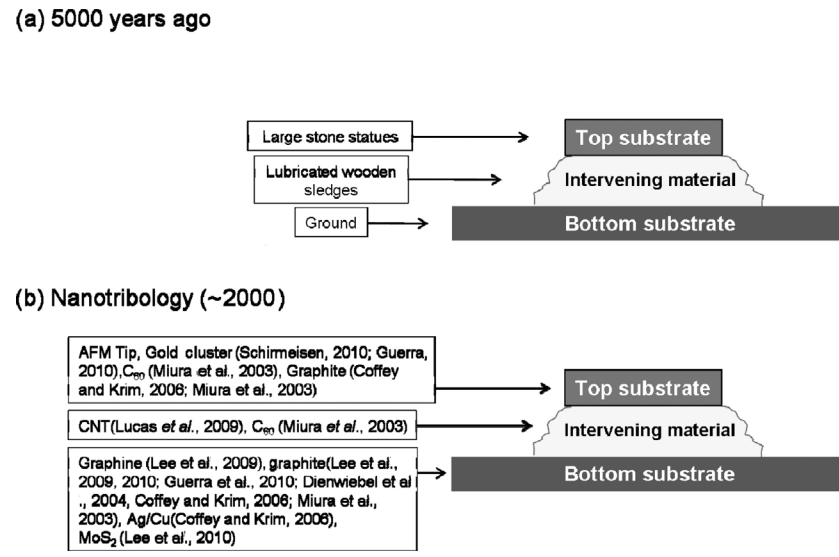

Figure 6 Schematic descriptions of examples in tribological advances: (a) transportation of large stone statues in Egypt (5000 years ago) and (b) nanotribology of dry surfaces (~2000).

surface. His notebooks remained unpublished for hundreds of years. Later, Amontons's and Coulomb's classical microscopic friction laws have far outlived a variety of attempts to explain them on a fundamental basis in terms of, say, molecular adhesion (attraction between particles in the opposing surfaces). Nowadays, the surface consists of many forms of carbons (hydrogenated or nitrogenerated carbon, C_{60}, carbon nanotube (CNT), and graphene) as illustrated in Figure 6b. Many efforts have been made to understand atomistic dry surfaces for nanotribology including superlubricity (Figure 7) (Coffey and Krim, 2006; Dienwiebel *et al*., 2004; Guerra *et al*., 2010; Lee *et al*., 2009, 2010; Lucas *et al*., 2009; Miura *et al*., 2003; Schirmeisen, 2010). In this paper, we focus on our effort in HDD dealing with wet, meso-scale surfaces (Figure 8a).

HDDs have been one of the most dominant data storage systems with high-density recording capacity yet relatively low cost. Thus, the information technology area widely utilizes HDD as a main storage system and its application is currently extended to consumer personal electronics and portable devices. As shown in Figure 8b, HDD is mainly composed of several parts: magnetic read/write heads and magnetic disks (platters), data detection electronics and write circuit, mechanical servo and control system, and interface to microprocessor. A stack of 3–10 disk platters, each containing a layer of magnetic medium, is attached to a motor spindle, which rotates the stack at

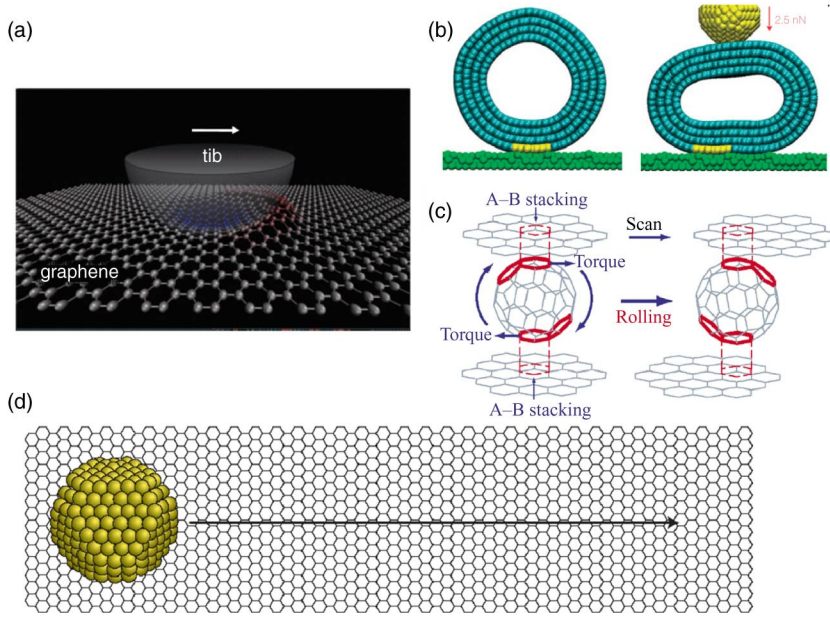

Figure 7 Examples of nanotribology on dry carbon surfaces for atomic force microscopy (AFM): (a) schematic description of the out-of-plane graphene deformation with the sliding AFM (Lee et al., 2010), (b) nanotube without tip (left) and tip–nanotube interaction under 2.5 nN normal force (right) (Lucas et al., 2009), (c) stick–slip rolling model with a step rotation of a C_{60} molecule (Miura et al., 2003), and (d) ballistic sliding of gold nanocluster on graphite (Schirmeisen, 2010).

speeds of 5,000 to over 15,000 revolutions per minute (RPM). The read/write head is located on the trailing edge of the head, which is mounted at the end of the actuator arm, via a servo, which can precisely control the radial position of the read/write heads to access data on the rotating hard disk platters.

The actual magnetic processes for the recording occur in the head-disk interface (HDI) as schematically described in Figure 9, consisting of flying read/write head and the disk (substrate, underlayer, magnetic layer, carbon-overcoat, and lubricant layer) (Johnson *et al.*, 1996). The substrate of choice is aluminum because of its low density and low cost. However, aluminum by itself is quite soft. Therefore, electroless nickel–phosphorus-plated (Ni–P) aluminum is universally used today to provide a hard surface for magnetic film structural support as well as the capability of being polished to a high degree of smoothness for low-flying recording heads. The chromium (Cr) underlayer serves to help

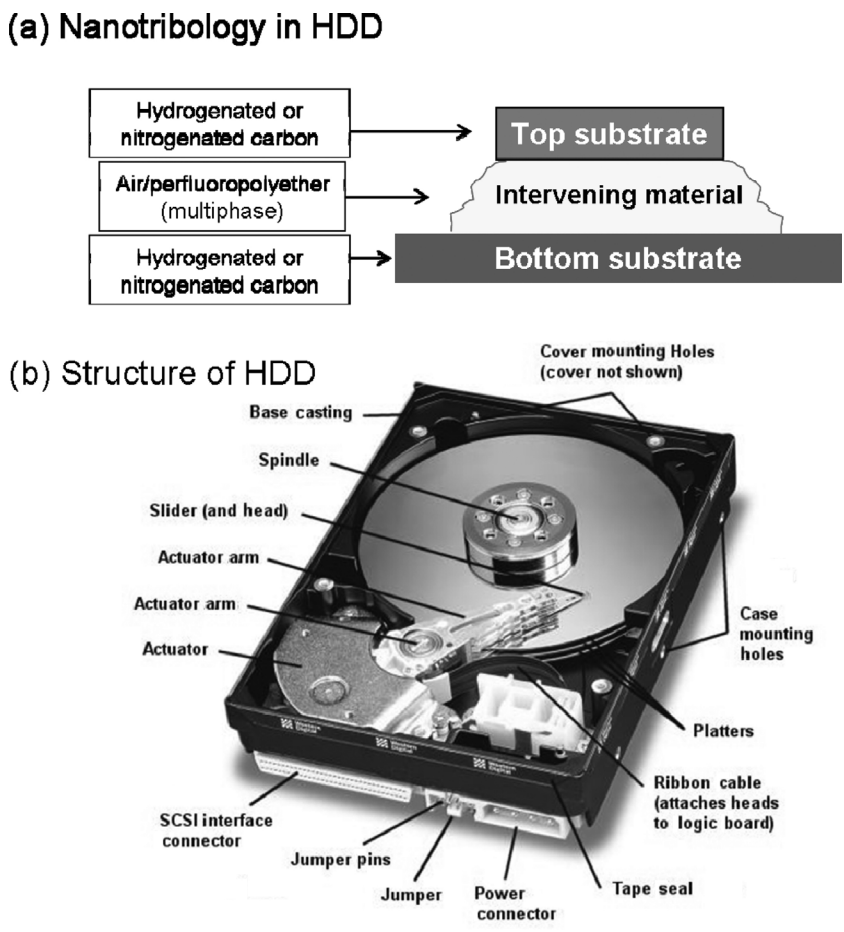

Figure 8 (a) Nanotribology in HDD and (b) a typical HDD system.

nucleate and grow the microstructure of appropriate magnetic properties because of an epitaxial match between the Cr planes and the cobalt (Co)-based magnetic alloys in the thin film media. Although Co by itself has a very low coercivity, Co-based binary and ternary alloys are suitable for the ferromagnetic material in the magnetic layer, since they provide a high coercivity that can even be tailored by varying the alloy composition. Cr is a crucial second or third element here as can reduce corrosion potential and allow for precipitation of other crystalline phases at grain boundaries or within grains to reduce noise. The plasma enhanced chemical vapor deposition (PECVD) amorphous carbon-overcoat is sputtered over the magnetic layer, because it seals the data

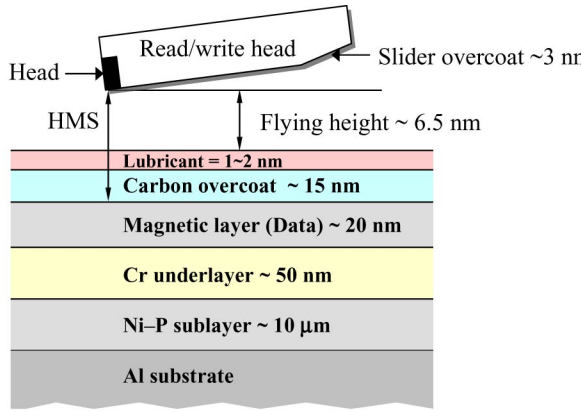

Figure 9 The cross-sectional diagram of a typical HDI for a HDD system with aluminum substrate.

layer from corrosion and chemical surface deformity, protects the data layer from physical damage during the intermittent contact between the head and the disk, and minimizes the thermally induced erasure of data bits due to the heat transfer to the data layer in the event of a head-disk contact.

The lubricant film is essentially the first line of protection from the mechanical damage in the event of intermittent contact between head and disk, and serves to reduce the friction and wear between carbon-overcoat and the recording head. It brings additional stability to the HDD by providing the recording heads a smooth transition from a region of dragging to flying and by adsorbing some of the energy that is generated by the head-disk contact. An ideal lubricant candidate is expected to possess chemical inertness to avoid chemical reaction, low vapor pressure to prevent evaporation loss, low surface tension to allow its uniform wetting on the overcoat for the near-field recording, high stability under shear stress to avoid degradation, and good boundary lubrication properties (Klaus and Bhushan, 1985). It is equally important that the lubricant should present appropriate chemical affinity for the overcoat and can reside on the disk surface over the HDD lifetime without desorption, spin-off, and thermal degradation (Karis *et al.*, 2001; Tani and Matsumoto, 2003; Tyndall *et al.*, 1999). On the other hand, a reasonable lubricant diffusion capability is also expected for the ''self-healing'' purpose in the event of head-disk contact, where lubricant depleted zones may be formed and thus cause a possible head crash. The current commercialized lubricant for HDD industry is a class of

Table 1 The endgroup structure, number averaged molecular weight (M_n), and relevant physical properties of Fomblin Z derivatives

Fomblin Z	Endgroup (X) structure	M_n, g/mol	Kinematic viscosity at 20°C (St)	Vapor pressure, Torr		Surface tension at 20°C
				20°C	100°C	
Z03	$-CF_3$	4000	0.3	/	/	23
Zdol	$-CF_2CH_2OH$	2000	0.85	2×10^{-5}	2×10^{-5}	24
Ztetraol	$-CF_2CH_2OCH_2$ -CHOH-CH_2 -OH	2200	20	5×10^{-7}	2×10^{-4}	/
Zdol-TX	$-CF_2CH_2(OCH_2CH_2)_pOH$	2100	1.45	2×10^{-5}	2×10^{-3}	23
AM2001		2400	0.75	1×10^{-7}	2×10^{-5}	25
A20H	HO– and/or	3000	/	/	/	22

oligomeric, random linear copolymers named PFPEs with the chemical structure of

$$X-[(OCF_2CF_2)_p-(OCF_2)_q]-O-X\,(p/q \cong 2/3).$$

Here, X stands for the functional endgroup. Its weight average molecular weight (M_w) ranges from 2000 to 4000 g/mol. PFPE Z03 has nonfunctional endgroup ($X = CF_3$), while its derivatives, PFPE Zdol and Ztetraol, have the functional endgroups ($X = CF_2CH_2OH$ for Zdol and $X = CF_2CH_2CH(OH)CH_2OH$ for Ztetraol). Here, the hydroxyl groups in the chain ends determine the functionality of PFPEs. The detailed physical properties of various PFPEs are provided in Table 1.

The interaction between PFPEs and disk overcoat is another significant factor to affect the properties of lubricant films. PFPEs with functional endgroups (e.g., Zdol and Ztetraol) perform better than PFPEs with nonfunctional endgroup (e.g., Z03) for retention and evaporation at the expense of the surface mobility or replenishment ability. However, strong endgroup functionality can lead to the layering and instability (e.g., surface nonuniformity/dewetting) of PFPE films (Karis

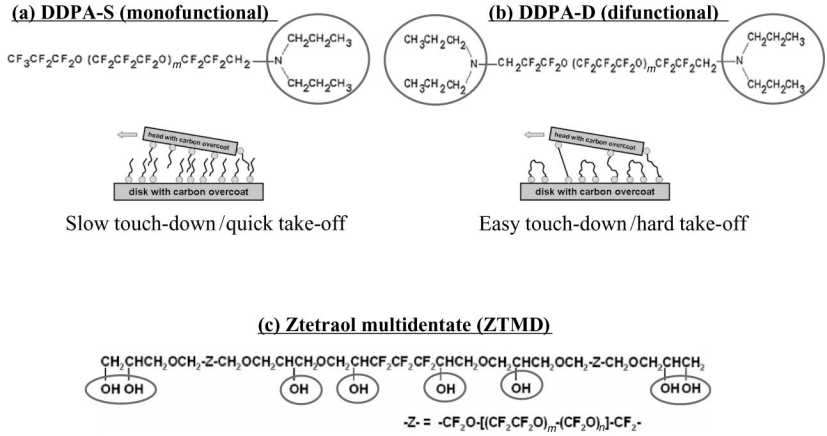

Figure 10 The molecular structure of recently reported lubricants: (a) DDPA-S, (b) DDPA-D, and (c) ZTMD for ultrasmall HMS.

et al., 2005; Waltman *et al*., 2002). This interaction can also be tuned via modifying the surface functionality of carbon-overcoat by introducing dopants such as hydrogen and nitrogen into the vacuum chamber during the sputtering process (Lee *et al*., 1993; White *et al*., 1996). To date, the bonding mechanism between PFPEs and overcoat was investigated via electron spin resonance (ESR) or time of flight secondary ion mass spectroscopy (TOF-SIMS), where it is postulated that a hydrogen atom is transferred from a hydroxyl group in Zdol chain end to a dangling bond site on the carbon film (Kasai, 2002; Kasai and Spool, 2001; Kasai *et al*., 1999; Zhu *et al*., 2003). The *ab initio* calculation suggested the possible hydrogen bonding interaction (Waltman *et al*., 1999a), while annealing can also lead to the esterification (Waltman *et al*., 1998). Recently, new types of lubricants, whose chemical structures are shown in Figure 10, have been reported to enhance the performance and reliability of HDD with ultrasmall head-medium spacing (HMS). Researchers introduced new functional group, dipropylamine, in the Demnum chain end. Both monofunctional (DDPA-S) and difunctional (DDPA-D) were synthesized and characterized (Sakane *et al*., 2006). It was found that DDPA-S can significantly reduce the head-disk adhesive interaction at near-contact operation as shown in Figure 10, which is believed to be a promising lubricant for ultrasmall HMS. With the additional functional groups in the center of PFPE chain, Ztetraol multidentate (ZTMD) can form additional anchors on the overcoat surface and be suitable for HMS less than 5 nm (Guo *et al*., 2006; Marchon *et al*., 2006).

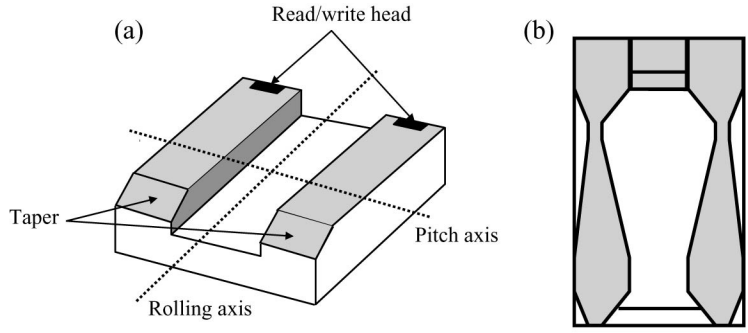

Figure 11 A schematic of (a) IBM 3370 and (b) negative pressure heads.

In the current HDDs, the read/write head flies about 6.5 nm above the surface via the air bearing design. Earlier models of head featured two straight and flat rails having a taper at the front, known as positive pressure head, for example, IBM 3370 head (Figure 11a). Air is compressed in the taper region of the head, creating an air bearing that supports the head above the surface of the disk. Negative or subambient pressure heads (Figure 11b) are introduced to reduce the normal load, while maintaining the stiffness of positive pressure designs. The aerodynamic operation of negative pressure heads can be explained from consideration of positive and negative pressure region. The side rails of the head generate a positive pressure, which tend to separate the head from the disk. The main recessed region confined by a cross rail and side rails produces a suction force that attracts the head to the disk. Negative pressure heads generally exhibit favorable characteristics of low normal load, high air bearing stiffness, and better altitude performance. Naturally, one might come up with a way to reduce fly height by permitting the head to slide over the disk surface (so-called contact recording) much like the head for a tape drive. To use this zero-spacing approach, there are still many technological hurdles to be resolved, such as protecting the head and the disk from heat generation, high friction, and wear. Instead of achieving full contact, liquid bearing technology (Lemke *et al*., 1994), where a viscoelastic liquid is fully flooded in the HDI instead of compressible air, has been proposed.

In HDI, the head flies above the disk surface with the fluid mechanics of air bearing generated by the rotation of disks at high speeds. Contact between the head and the disk occurs during the cycles of the operation start/stop and intermittently during disk operation due to the fluctuation of the fly height. Since the fly height has been reduced to ~6.5 nm, the head can even interact with the disk surface via van der

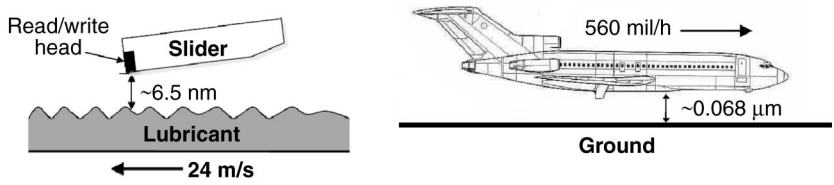

Figure 12 A magnetic head slider flying over a disk surface (slider located on the position 1.25 in. from the disk center rotating in 7600 rpm) compared with an aircraft flying in 560 mile/h over ground with a close physical spacing.

Waals interaction, which induces the growth of roughness of lubricant surface (Pit *et al.*, 2001). Figure 12 helps understanding a degree of a close physical spacing of HDI via geometric comparison of an aircraft flying over ground although nanoscale phenomena cannot be explained by scaling up to macroscale. As coercivity and areal density of magnetic layer define the HDD capacity, HDI determines the stability and durability, which cause the tribological issues due to the mechanical contact. Since magnetic recording is a nanoscale near-field process, it is essential to maintain a stable interface in the proximity recording for the long-term reliability of HDDs. In addition, to increase the areal density, each component in HMS must be reduced in dimension, which places significant constraints on both head and disk parameters. Therefore, current HDD demands intensive research and development on the system stability and reliability, which can be enhanced by multi-scale approaches on the lubricant molecules, carbon-overcoat on the magnetic layer, and read/write head (via shape optimization to obtain reliable and constant flying).

3. STRUCTURE OF HIERARCHICAL EQUATIONS

During the past few decades, various theoretical models have been developed to explain the physical properties and to find key parameters for the prediction of the system behaviors. Recent technological trends focus toward integration of subsystem models in various scales, which entails examining the nanophysical properties, subsystem size, and scale-specified numerical analysis methods on system level performance. Multi-scale modeling components including quantum mechanical (i.e., density functional theory (DFT) and *ab initio* simulation), atomistic/molecular (i.e., Monte Carlo (MC) and molecular dynamics (MD)), mesoscopic (i.e., dissipative particle dynamics (DPD) and lattice Boltzmann method (LBM)), and macroscopic (i.e., LBM, computational

fluid mechanics, and system optimization) descriptions have also gained tremendous attention. Here, we will explain the general modeling methods and the structure of hierarchical equations, which are broadly utilized in multi-scale approaches. System specified modification of each modeling method will be discussed in the next chapter.

3.1 Quantum level

Theoretical models at the quantum level are important ingredients in the multi-scale modeling strategy, since the techniques do not require empirical knowledge for effective calculation. At this level of scale, the molecular system is described by utilizing various *ab initio* quantum mechanical calculations, which are currently available to solve many body wave-function problems represented by the Schrödinger equation (Jensen, 1999). The DFT is an alternative method to reduce the computational load by using energy functionals depending on the density of the particles (Parr and Yang, 1989). In this calculation, the ground-state electronic energy is determined by the electron density representing the correspondence between the electron density and the energy (Hohenberg and Kohn, 1964). Although the quantum level calculation promises accuracy since the model is based on the fundamental and nonempirical rules, the calculation demands a huge computational cost; as a consequence the technique cannot be utilized for the upper level of the scale represented as massive molecular systems, which are more than approximately 1000 atoms. Therefore, quantum level models are generally utilized with a combination of molecular-level theories. For instance, Leconte *et al*. (2010) investigated the electronic and transport properties of ozone-treated graphene by using multi-scale *ab initio* with a real space order-N transport computational methodology based on a reparameterized tight-binding Hamiltonian. Many researchers have pursued a multi-scale computational approach to the theoretically inspired optimization of the electroactive properties of organic and hybrid materials (Dalton *et al*., 2007; Kim *et al*., 2008; Olbricht *et al*., 2008; Pereverzev *et al*., 2008; Sullivan *et al*., 2007). Most recently, this approach has evolved into a correlated quantum/statistical mechanical approach based on improvements to real-time, time-dependent density functional theory (RTTDDFT) and pseudo-atomistic Monte Carlo/molecular dynamics (PAMCMD) calculations (Dalton, 2009). While the initial target for this effort was the transformative improvement of organic electrooptic materials, theoretical approach is also relevant to developing improved organic electronic, light emitting, photorefractive, and most particularly organic photovoltaic materials. Although DFT presented an advantage in the balance of computational cost and

accuracy in quantum mechanics calculations, the method cannot accurately handle the ubiquitous dispersion interactions (London dispersion forces), which is difficult to describe most of theoretical models including *ab initio* calculation (Johnson and DiLabio, 2006; Kohn *et al*., 1998; Meijer and Sprik, 1996). Empirical atom–atom based correction terms of C_6/R^6-type are commonly used to determine the parameters (LeSar, 1984; Meijer and Sprik, 1996). Recently, DFT for dispersion interaction has been investigated including parameterized functionals and dispersion-correcting potentials (Johnson *et al*., 2009).

At this level, we note that we can obtain first-principles (no adjustable parameters) prediction of properties such as electrooptic activity in complex organic and hybrid materials. Organic and hybrid materials have been also integrated within silicon electronic and photonic device structures, and it enables theoretical analysis of the performance of these novel device architectures, which involve enormous enhancement of optical and electric fields. This work provides a proof of concept that detailed quantum mechanical methods can be used to inform macroscale experimental systems, producing new materials with dramatically improved properties. In the field of PEFC and HDI, quantum chemical modeling based on atomistic simulation was introduced extensively to investigate the perfluoro polymeric systems (i.e., PEM and PFPE) and the interactions of their functional bodies (Goddard *et al*., 2006; Waltman *et al*., 1999a, 1999b).

3.2 Atomistic/molecular level

Classical molecular simulation methods such as MC and MD represent atomistic/molecular-level modeling, which discards the electronic degrees of freedom while utilizing parameters transferred from quantum level simulation as force field information. A molecule in the simulation is composed of beads representing atoms, where the interactions are described by classical potential functions. Each bead has a dispersive pair-wise interaction as described by the Lennard–Jones (LJ) potential, $U_{\mathrm{LJ}}(r_{ij})$:

$$U_{LJ}(r_{ij}) = 4\varepsilon_{ij}\left[\left(\frac{\sigma}{r_{ij}}\right)^{12} - \left(\frac{\sigma}{r_{ij}}\right)^{6}\right], \tag{1}$$

where σ is the diameter of beads, ε_{ij} corresponds to the well depth of LJ interaction, r_{ij} denotes the distance between two beads i and j. To model the electrostatic effects, the nonbonding interactions were modified by

the combination of van der Waals interaction and the electrostatic Coulombic interaction:

$$U_{LJ-C}(r_{ij}) = 4\varepsilon_{ij}\left[\left(\frac{\sigma}{r_{ij}}\right)^{12} - \left(\frac{\sigma}{r_{ij}}\right)^{6}\right] + \frac{q_i q_j e^2}{4\pi\varepsilon_0}\frac{1}{r_{ij}} \tag{2}$$

where, ε_0 is the dielectric constant of vacuum, e represents elementary electric charge, and q_i and q_j are the charge parameters for Coulombic interaction. Chemical bond between adjacent beads is commonly represented by harmonic potential energy:

$$U_r = (1/2)K_r(r - r_o)^2 \quad \textit{and} \quad U_\theta = (1/2)K_\theta(\theta - \theta_0)^2 \tag{3}$$

where U_r and U_θ are the stretching and bending potentials, respectively, K_r is the stretching force constant, K_θ is the bending force constant, r_o is the equilibrium bond length, and θ_o is the equilibrium angle. The stretching interactions take place between two bonded atoms, while the bending accounts for the bending of the angle formed by two adjacent bonds. Alternatively, anharmonic finitely extensible nonlinear elastic (FENE) springs connect the adjacent beads separated by a distance of r_{ib}:

$$U_{FENE}(r_{ib}) = \begin{cases} -\frac{1}{2}kR_0^2 \ln\left[1 - \left(\frac{r_{ib}}{R_0}\right)^2\right] & r_{ib} < R_0 \\ \infty & otherwise \end{cases}. \tag{4}$$

Here, r_{ib} denotes the interbead distance (i.e., the bond length between two adjacent beads), k is the spring constant that quantifies the rigidity of the bond, and R_0 is the maximum extensibility of the spring. The form of torsional potential parameters, describing four bonded atoms, is

$$U_\phi = k_\phi \sum_{n=0}^{N-1} A_n \cos^n \phi \tag{5}$$

where U_ϕ is the torsional potential, k_ϕ is a constant, A_n are the torsional potential coefficients, and ϕ is the torsional angle. To incorporate classical potential functions with quantum mechanical calculations, eigenvalue analysis is developed to calculate stretching and bending parameters from the *ab initio* Hessian matrix for the harmonic potential form, and the torsional potential parameters are calculated by generating the *ab initio* torsional energy profiles via a series of constrained geometry optimization.

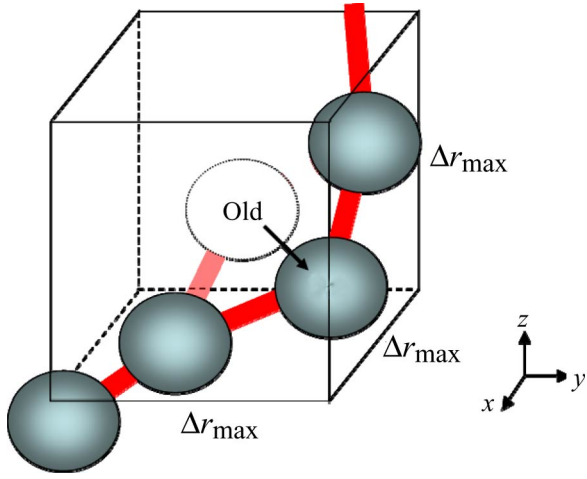

Figure 13 A trial movement is generated in a cube with a dimension of r_{max} centered by the selected bead. Red line represent skeletal bond.

MC, which is a time-independent molecular simulation, utilizes the stochastic motion of the bead to measure the static properties or to equilibrate the system before measuring time-dependent dynamic properties using MD due to its advantages in computational cost. A single bead is selected randomly for the MC trial movement during each attempt. The displacement vector is set randomly in a cube centered by the selected bead as shown in Figure 13 ($\mathbf{r} = x\mathbf{i} + y\mathbf{j} + z\mathbf{k}$ with $-r_{max} / 2 < x, y, z < r_{max} / 2$). Here, $\mathbf{r}$ denotes the position vector of beads, $\mathbf{i}$, $\mathbf{j}$, and $\mathbf{k}$ are unit vectors in x, y, and z directions, and r_{max} is the maximum displacement allowable in the trial movement. For each trial movement, the total potential energy difference before and after the trail movement is calculated from the system potential energies as follows:

$$U_{total} \equiv U_{inter} + U_{intra} \tag{6}$$

where U_{inter} and U_{intra} represent intermolecular (e.g., LJ and Coulombic interactions) and intramolecular (e.g., stretching, bending, and torsion) energies, respectively. The acceptance of a trial move is determined by the probability distribution law based on the detailed balance to keep the system in equilibrium. Metropolis acceptance probability W determines whether the trial movement will be accepted or not (Frenkel and Smith, 2000; Metropolis *et al.*, 1953):

$$W = min[\exp(U^{total}/k_B T),\ 1]. \tag{7}$$

Here, k_B and T are the Boltzmann constant and absolute

temperature, respectively. When W exceeds a random number ranging between 0 and 1, the trial movement is accepted, and the position of bead is updated. Otherwise, the bead is placed back to the original position. The trial movement of beads will be repeated for enormous number of time steps, which depends on the system size, until the potential energy of the system approaches the statistical constant, indicating the equilibrium state. MC provides enormous advantages in calculation cost by comparing MD, which utilizes the dynamic equations, for novel algorithms and ensembles. These have been intensively investigated during past few decades for molecular-level analysis of complex phenomena including phase equilibria and massively entangled polymeric systems (Theodorou, 2010).

The molecular motion in MD simulation is deterministic by solving a Hamiltonian system (Allen and Tildesley, 1996). For the precise description of the polymeric systems, Langevin dynamics (Grest, 1996) were employed, where the force acting on the ith bead in the αth molecule can be calculated by the following equation:

$$m\frac{d^2 r_{\alpha i}}{dt^2} = -\frac{\partial U}{\partial r_{\alpha i}} - \zeta \cdot \frac{dr_{\alpha i}}{dt} + f^*_{\alpha i}(t). \tag{8}$$

Here, m and $\mathbf{r}_{\alpha i}$ are the mass and position vector of beads, respectively. ζ is the friction tensor, which is assumed to be isotropic for simplicity in our simulation, that is, $\zeta = \Gamma I$, where I is the unit dyad and $\Gamma = 0.5\tau^{-1}\left(\tau = \sigma(m/\varepsilon)^{0.5}\right)$ (Grest, 1996). Further, $f^*_{\alpha i}$ is the Brownian random force, which obeys the Gaussian white noise, and is generated according to the fluctuation–dissipation theorem:

$$\langle f^*_{\alpha i}(t) f^*_{\beta j}(t')\rangle = 2k_B T \delta_{\alpha\beta} I \delta_{ij} \delta(t - t'), \tag{9}$$

where the angular bracket denotes an ensemble average. $\delta_{\alpha\beta}$ and δ_{ij} are Kronecker deltas, and $\delta(t - t')$ is a Dirac's delta function. T and quantify the magnitude of Brownian force. Langevin equation is a phenomenological stochastic differential equation of motion describing time evolution of a subset of the degrees of freedom for slowly relaxing (macroscopic) variables while the rapidly relaxing (microscopic) variables, which result in the stochastic nature in the equation. Langevin equations can be systematically derived via standard Mori and Zwanzig projection operator method (Hijón *et al.*, 2010) by projecting out fast degrees of freedom (irrelevant variables contained in fluctuating random force, f). The dynamics of relevant variables are described by potential energy calculated from quantum mechanics and information containing irrelevant variables through f or equivalently, ζ, which are related by fluctuation–dissipation theorem shown in Equation (9).

Using EMD simulations, transport properties can be obtained via the Green–Kubo linear response theory and the corresponding time correlation functions. However, one of the main concerns for EMD method is that the fluctuations naturally occurring in the equilibrated system are fairly small. As a result, the signal-to-noise ratio (SNR) is very unfavorable at large time range, where the time correlation functions exhibit long tails giving a significant contribution to the integrals defining the corresponding transport properties. However, if we can introduce much larger fluctuations artificially, the SNR of the measured response may be improved dramatically. Therefore, nonequilibrium molecular dynamics (NEMD) is introduced to study the nonequilibrium dynamics such as rheological properties. Historically, the first fictitious force method proposed for simulating viscous flow was the Doll's tensor method (Hoover *et al*., 1980) as shown in Equation (10), which can be derived from the Doll's tensor Hamiltonian.

$$\begin{aligned} \frac{d\mathbf{r}_{\alpha i}}{dt} &= \frac{1}{m}\mathbf{p}_{\alpha i} + \mathbf{r}_{\alpha i}\cdot\nabla\mathbf{u} \\ \frac{d\mathbf{p}_{\alpha i}}{dt} &= -\frac{\partial U}{\partial \mathbf{r}_{\alpha i}} - \nabla\mathbf{u}\cdot\mathbf{p}_{\alpha i}. \end{aligned} \tag{10}$$

Here, $\mathbf{p}_{\alpha i}$ is the bead momentum vector and $\mathbf{u}(\mathbf{r}_{\alpha i}, t) = \mathbf{i}\gamma r_{\alpha i}^{y}$ is the linear streaming velocity profile, where $\gamma \equiv \partial u_x/\partial y$ is the shear strain rate. Doll's method has now been replaced by the SLLOD algorithm (Evans and Morriss, 1984), where the Cartesian components that couple to the strain rate tensor are transposed (Equation (11)).

$$\begin{aligned} \frac{d\mathbf{r}_{\alpha i}}{dt} &= \frac{1}{m}\mathbf{p}_{\alpha i} + \mathbf{r}_{\alpha i}\cdot\nabla\mathbf{u} \\ \frac{d\mathbf{p}_{\alpha i}}{dt} &= -\frac{\partial U}{\partial r_{\alpha i}} - \mathbf{p}_{\alpha i}\cdot\nabla\mathbf{u}. \end{aligned} \tag{11}$$

With $\mathbf{u}(\mathbf{r}_{\alpha i}, t) = \mathbf{i}\gamma\mathbf{r}_{\alpha i}^{y}$, Equations (11) is equivalent to

$$m\frac{d^2\mathbf{r}_{\alpha i}}{dt^2} = -\frac{\partial U}{\partial \mathbf{r}_{\alpha i}} + \mathbf{i}m\frac{d\gamma}{dt}\mathbf{r}_{\alpha i}^{y}. \tag{12}$$

Both the Doll's and SLLOD algorithms are correct in the limit of zero-shear rate. However, for finite shear rates, the SLLOD equations are exact but Doll's tensor algorithm begins to yield incorrect results at quadratic order in the strain rate, since the former method has succeeded in transforming the boundary condition expressed in the form of the local distribution function into the form of a smooth mechanical force, which appears as a mechanical perturbation in the equation of motion (Equation (12)) (Evans and Morriss, 1990). To thermostat the

SLLOD algorithm, the thermostat Gaussian multiplier ψ is introduced:

$$\begin{aligned}\frac{d\mathbf{r}_{\alpha i}}{dt} &= \frac{1}{m}\mathbf{p}_{\alpha i} + \mathbf{r}_{\alpha i}\cdot\nabla\mathbf{u} = \frac{1}{m}\mathbf{p}_{\alpha i} + \mathbf{i}\gamma\mathbf{r}^{y}_{\alpha i}\\ \frac{d\mathbf{p}_{\alpha i}}{dt} &= -\frac{\partial U}{\partial \mathbf{r}_{\alpha i}} - \mathbf{p}_{\alpha i}\cdot\nabla\mathbf{u} - \psi\mathbf{p}_{\alpha i} = -\frac{\partial U}{\partial \mathbf{r}_{\alpha i}} - \mathbf{i}\gamma\mathbf{p}^{y}_{\alpha i} - \psi\mathbf{p}_{\alpha i}.\end{aligned} \tag{13}$$

In the isokinetic version of the algorithm, where the total kinetic energy $\sum_\alpha \sum_i \mathbf{p}^2_{\alpha i}/2m$ is held constant, ψ is given by

$$\psi = \sum_\alpha \sum_i \left(-\frac{\partial U}{\partial \mathbf{r}_{\alpha i}}\cdot\mathbf{p}_{\alpha i} - \gamma\mathbf{p}^{x}_{\alpha i}\mathbf{p}^{y}_{\alpha i}\right) \Big/ \sum_\alpha \sum_i \mathbf{p}^2_{\alpha i}. \tag{14}$$

To bridge the time-scale gap between microscopic and macroscopic scales and accurately capture dynamic phenomena on the coarse-grained level, systematic time-scale-bridging molecular dynamics was recently introduced by using an alternative MC–MD iteration scheme, which also shows higher calculation efficiency than standard NEMD (Ilg *et al*., 2009).

3.3 Meso-scale/continuum level

LBM was introduced as an alternative meso-scale/continuum-level modeling tool, which has the advantages in capturing clear physics in the system with the complex geometry and nanoscale physics. Since LBM covers broad range of the system scale and is based on the particle assumption, the method is considered as a multi-scale method from meso-scale to continuum scale including buffer region simulation to substitute computational fluid dynamics as well as a promising candidate for hierarchical integration with atomistic/molecular-level models. Physical phenomena in air bearings/viscoelastic liquid bearings in the HDI system and heat transfer phenomena have been modeled via LBM (Ghai *et al*., 2005, 2006a, 2006b; Kim *et al*., 2005a, 2005b). Especially, due to the convenience of complex geometry manipulation, LBM is suitable for modeling flow in porous media, which can be utilized for GDL simulation in PEFC.

LBM has emerged as a promising numerical tool for simulating fluid flows and thermal management with complex physics (Chen and Doolen, 1998). The numerous advantages including clear physical pictures, an inherently transient nature, multi-scale simulation capabilities, and fully parallel algorithms make LBM to be an attractive candidate as a multi-scale simulation tool. Kim *et al*. (2005a, 2005b) have developed a novel LBM by adopting a spatially dependent relaxation time model to predict the nanoscale air bearing performance. Unlike conventional numerical methods, which discretize the macroscopic equations, LBM

constructs simplified kinetic models incorporating the essential physics of microscopic processes so that the macroscopic properties obey the desired equations. The two-dimensional, lattice Boltzmann kinetic equation (LBKE) with Bhatnagar–Gross–Krook (BGK) approximation can be written as (Mei *et al.*, 2000)

$$f_i(\mathbf{x} + \mathbf{c}_i\, t, t + t) = f_i(\mathbf{x}, t) - \frac{1}{\tau}[f_i(\mathbf{x}, t) - f_i^{eq}(\mathbf{x}, t)] \quad \text{for } i = 0, 1, \ldots, N \tag{15}$$

where τ is the single relaxation time, which controls the rate of approach to equilibrium; $f_i(\mathbf{x}, t)$ is the discrete one particle distribution function, which is the probability of finding a particle with the velocity c_i at $(\mathbf{x}, t)$; t is the time step; N is the number of discrete particle velocities in each node, which is chosen to be 9 for D2Q9 (i.e., two-dimension and 9 directions of streaming) model used in this simulation; $f_i^{eq}(x, t)$ is the discrete equilibrium distribution function given as

$$f_i^{eq}(\mathbf{x}, t) = w_i \rho \left[1 + \frac{\mathbf{e} \cdot \mathbf{v}}{c^2} + \frac{\mathbf{vv} : (\mathbf{e}_i \mathbf{e}_i - c^2 \mathbf{I})}{2c^4}\right]$$
$$\text{with } w_i = \begin{cases} 4/9, & i = 0 \\ 1/9, & i = 1, \ldots, 4 \\ 1/36, & i = 5, \ldots, 8 \end{cases} \tag{16}$$

where v is the fluid velocity, $c \equiv s/t = \sqrt{3k_B T/m}$ is the lattice speed, Δs

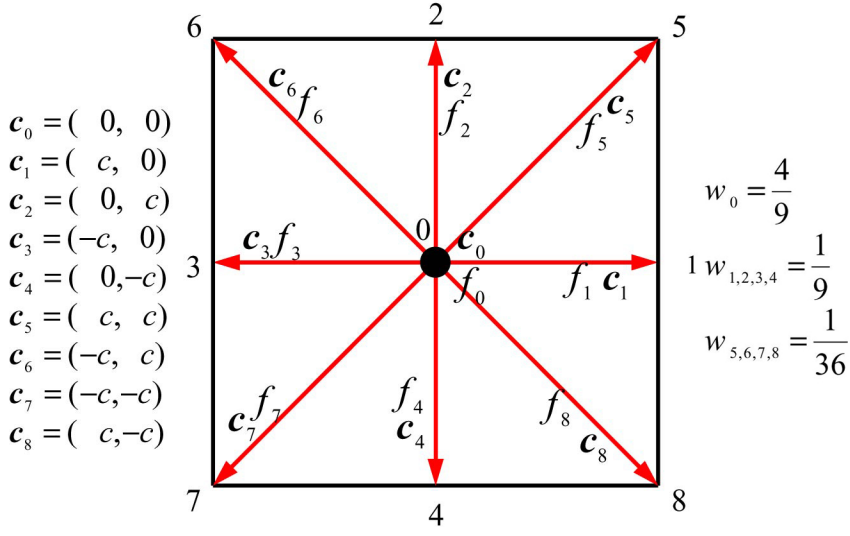

Figure 14 A lattice node of D2Q9 model (2D lattice with 9 directions of streaming)

is the lattice spacing, k_B is the Boltzmann constant, T is the fluid temperature, and m is the particle mass. The 9 discrete velocities in D2Q9 model (Figure 14) are given by

$$c_i = \begin{cases} (0,0),\ i = 0 \\ (\pm 1, 0)c, (0,\ \pm 1)c,\ i = 1, \ldots, 4 \\ (\pm 1,\ \pm 1)c,\ i = 5, \ldots, 8. \end{cases} \tag{17}$$

The density ρ and $\mathbf{v}$ are calculated by

$$\rho(\mathbf{x}, t) = \sum_i f_i \quad \textit{and} \quad \mathbf{v}(\mathbf{x}, t) = \frac{1}{\rho(\mathbf{x}, t)} \sum_i c_i f_i \tag{18}$$

In order to integrate polymeric systems via bridging among mesoscale/continuum scales, LBM and atomic/molecular scales, MD, and macroscopic scales, intermediate level models may be required. These maintain the nature of polymeric system with or without functional groups and provide coarse-grained levels that can be integrated to LBM. In Section 4.2, we provide a simple reactive sphere (SRS) model, which is one of the intermediate levels of system integration for reactive functional endgroups.

3.4 Process-scale level

Process-scale models represent the behavior of reaction, separation and mass, heat, and momentum transfer at the process flowsheet level, or for a network of process flowsheets. Whether based on first-principles or empirical relations, the model equations for these systems typically consist of conservation laws (based on mass, heat, and momentum), physical and chemical equilibrium among species and phases, and additional constitutive equations that describe the rates of chemical transformation or transport of mass and energy. These process models are often represented by a collection of individual unit models (the so-called unit operations) that usually correspond to major pieces of process equipment, which, in turn, are captured by device-level models. These unit models are assembled within a process flowsheet that describes the interaction of equipment either for steady state or dynamic behavior. As a result, models can be described by algebraic or differential equations. As illustrated in Figure 3 for a PEFC-base power plant, steady-state process flowsheets are usually described by lumped parameter models described by algebraic equations. Similarly, dynamic process flowsheets are described by lumped parameter models comprising differential-algebraic equations. Models that deal with spatially distributed models are frequently considered at the device

level, with partial differential equations that model fluid flow, heat and mass transfer and reactions. These are usually considered too expensive to incorporate within an overall process model. Process flowsheeting models, embodied in commercial process simulators such as ASPEN Plus®, HYSYS®, or PRO-II®, have become the accepted standard to describe and evaluate process engineering systems, for petroleum refineries, chemical processes, and power plants. Not only do they provide quantitative information on the flow of material and energy throughout a process network but they are used extensively to assess and analyze the current state of the process, improve the operation of existing processes, and guide and validate the design of new processes. As a result of their application in all of these engineering tasks, these process models have also become the medium of communication for crucial technical material shared among networks of project teams that participate in any engineering operation. On the other hand, simplifications used in process models (e.g., equilibrium-based, lumped parameter, and other short-cut models) often lead to inaccuracies and performance limitations.

Consequently, these models often require model tuning through semiempirical correlations and data integration. Such tasks are time-consuming and problem specific as they often require information from additional experiments and pilot plant trials, with missing information leading to start-up and operational risks. The incorporation of more accurate multi-scale phenomena (at device-, meso- and even molecular scales) captured by reduced-order models (ROMs) will overcome these limitations (Lang *et al*., 2009, 2011).

4. SYSTEM INTEGRATION

As introduced in the previous sections, multi-scale modeling can be realized via effective hierarchical analysis and simulation strategies correlating various models in different scales, where each level addresses specific physical phenomena (Gorban *et al*., 2006; Gubbins and Moore, 2010; Maginn and Elliot, 2010). The classical concept of the multi-scale modeling method is straightforward integration among the various scale levels, which utilizes the simultaneous description of all-scale subsystems. This method provides real-time multi-scale observation yet the computational time length depends on the slowest calculation. To overcome the disadvantage in the computational cost while retaining multi-scale advantages, the hierarchical multi-scale model, which utilizes parameters in lower level of scale to obtain new parameters for the upper level degree of freedom, has been investigated

(Theodorou, 2005; Ulherr and Theodorou, 1998). The hierarchical multi-scale model allows each level of calculation performed independently, and the input parameters can be estimated from other scale level models, which discard unnecessary calculations during the bridging procedure between the different scales (Delle Site and Kremer, 2005; Delle Site *et al.*, 2002, 2004; Doi, 2003; Glotzer and Paul, 2002). Recently, the focus of multi-scale modeling strategy is on developing bridging methodology connecting quantum–atomistic/molecular–meso-scale–continuum levels (Broughton *et al.*, 1999; Csanyi *et al.*, 2004; Delgado-Buscalioni and Coveney, 2003; Faller, 2004; Flekkoy *et al.*, 2000; Hadjiconstantinou, 1999; Laio *et al.*, 2002; Li *et al.*, 1998; Neri *et al.*, 2005; O'Connell and Thompson, 1995; Rafii-Tabar *et al.*, 1998; Smirnova *et al.*, 1999; Villa *et al.*, 2004).

4.1 Bridging methodology between different scale levels

The bridging procedure finds reduced-order parameters for upper level scale models. As shown in Figure 15, ROMs are introduced to capture the predictive behavior of the lower scale model and provide the links to capturing behavioral information from all of the lower scales, while

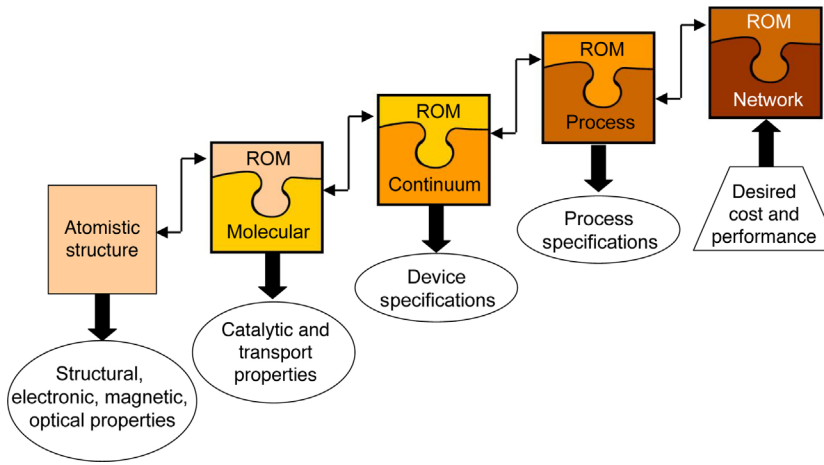

Figure 15 Linking models at various scales using ROMs and deriving lower scale specifications through an inverse optimization formulation. The ROM included at each scale is a reduced representation of the model at the scale below that could range from a set of parameters such as, for example, elementary rate constants to complex models derived from proper orthogonal decomposition and perhaps even to the full lower scale model. This is symbolized by coloring the ROM box with the same color as that of the box representing the adjacent lower scale model.

allowing the integrated formulation to be tractable. The major role of multi-scale ROMs is that they allow feasible realizations of complex domain models (consistency) and capture accurate complex model behavior over a wide range of the decision space (performance). With the development of ROMs at each level, modeling and optimization formulations at a given level will capture performance and feasibility at neighboring levels. By allowing this communication between levels, accurate and efficient decision making can be made. Also, note that the bidirectional flow between levels in Figure 15 easily allows us to develop and generalize ideas of reverse engineering and inverse problems.

The coupling of models at different scales is a challenging subject in the integration procedure, yet is most important for the accuracy of the multi-scale models. Especially the computational cost associated with large-scale calculations often precludes their integration over time and length scales, while rigorous models are now widely applied at all modeling scales. As an essential tool to overcome this barrier, ROM plays a critical role to link detailed phenomena at all modeling scales. While ROMs are widely applied over the entire modeling spectrum, their development is usually done as a one-time activity at an ad hoc level. In the development of a multi-scale modeling and optimization framework, it is required to develop a systematic approach for ROM development and integration. This will lead to the development of a single framework that promises much more detailed predictions of system-wide dynamics with high accuracy and interdependencies for large-scale decision making.

Depending on the particular length and time scale and the application domain, ROMs take a variety of different forms. Often, physics-based analytic models are derived from simplified, limiting behaviors of transport, reaction and equilibrium phenomena, and conservation laws. At the process engineering level, these lead to a rich and widely applied model library, which must nevertheless be extended to newer technologies in reaction and separation. Examples of these include macroscopic models for rate laws, vapor liquid equilibrium and thermodynamic properties used at the level of process networks. In addition, process models are often derived that consist of semiempirical functional forms fitted with data including reactor models and process models derived from data-derived correlations. At the device level, which is dominated by models in continuum mechanics, ROMs take a variety of forms, ranging from reduced-order solutions involving proper orthogonal decomposition (POD), variable resolutions models on meshes with varying degrees of refinement, variable-fidelity physics models such as inviscid, irrotational, and incompressible flow for

Navier–Stokes equations. Lastly, at atomistic and molecular levels, the task is to infer thermodynamic and kinetic properties and constants that are later used in macroscopic physics-based models. Often these calculations are used directly to regress to physics-based ROMs, such as with cluster expansion and kinetic MC modeling, or through coarse-grained models described below. Moreover, for complex device or molecular models, such as time consuming continuum mechanics and probabilistic models with little or no structural information, general regression-based model are derived that apply data-driven regression approaches (e.g., PCA, compressed sensing, neural nets, and wavelets). At all of these levels, ROMs have approximation errors that prevent their direct integration for multi-scale decision making. Nevertheless, uncertainty bounds can be developed along with these models, as described in Oberkampf *et al*. (2002) and Frenklach *et al*. (2002, 2004). These bounds lead to confidence regions in the parameter space of the ROM, which can be propagated through the multi-scale model hierarchy for the verification and validation task.

The overall approach introduces challenges for numerical methods, error estimates and linking with physics-based models. Moreover, with the availability of ROMs across the spectrum of relevant problem scales, one can develop multi-scale optimization formulations that act as the ''glue'' toward their integration, leading to the entire model. The following sections detail these formulations and discuss enabling algorithmic and computational technologies required to realize this integrated multi-scale framework.

4.2 Coarse-graining methods

4.2.1 Quantum—atomistic/molecular levels

From the equilibrium geometries in the quantum mechanical models, the atomistic intramolecular force field parameters, which are potential parameters in atomistic MD simulation, can be obtained by using the method of Seminario (1996). With the combination of atomistic MD simulation, quantum mechanical properties of the materials have provided the advances in the study of the fundamental phenomena in nanoscale. However, the processes at the device or system level occur above the microscale, where the quantum level as well as atomistic level cannot cover. Therefore, the development of a coarse-graining procedure, which simplifies the detailed structure of molecules while keeping the fundamental phenomena from quantum/atomistic level models, becomes one of the critical issues in atomistic/molecular-level modeling. Izvekov and Voth (2005a, 2005b) introduced the force-matching method for coarse-graining, which determines a coarse-graining

potential from atomistic information through a variational minimization procedure, and the method has been applied to the study of various material systems (Iuchi *et al*., 2007; Izvekov *et al*., 2005, 2006a, 2006b; Shi *et al*., 2006; Wang *et al*., 2006a; Zhou *et al*., 2007). Reverse Monte Carlo (RMC) techniques were introduced to simulate a particle system to produce the correct radial distribution function without the explicit need for a potential (McGreevy, 1995; McGreevy and Pusztai, 1988; Soper, 1996). The method was further extended to DNA studies by Lyubartsev and Laaksonen (1995). Reith *et al*. (2003) successfully developed coarse-grained modeling for the polymer by using iterative Boltzmann inversion. Further, the coarse-graining framework was expanded with a general statistical mechanical theory by introducing the many-body potential of mean force, which enables coarse-graining model consistent with atomistic models (Noid *et al*., 2008a, 2008b; Wang *et al*., 2006a). The coarse-grained sites are constructed by clusters of atoms where the mass of the coarse-grained site is the sum of the included atoms. The new coarse-grained bond lengths are calculated from the distance between the centers of mass of the clusters of atoms as shown in Figure 16.

The method aims to pass the distribution of structural parameters from the atomistic structure to the coarse-grained. The procedure involves performing an atomistic MD simulation and calculating the

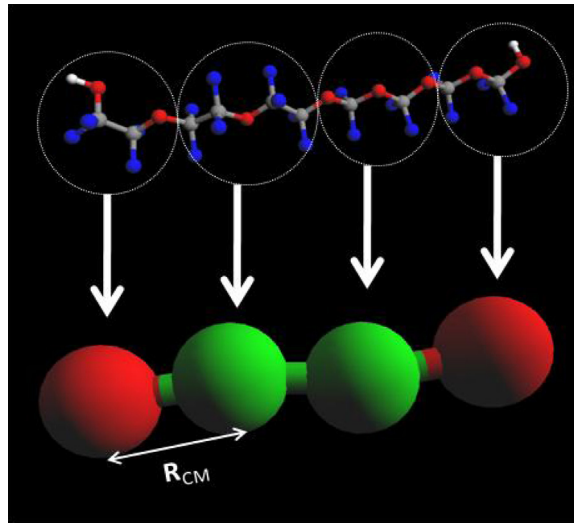

Figure 16 Mapping of atomistic clusters onto coarse-grained sites. R_{CM} represents the bond between coarse-grained sites, where the sites are the centers of mass of the atomistic clusters.

equilibrium probability distributions of the corresponding coarse-grained bond lengths, bond angles, and torsional angles. A Boltzmann distribution is fit to the distribution determined from the MD simulation by varying the parameters of the bonded potential:

$$P(r) \propto \exp(-U_r(r)/k_B T) \tag{19}$$

where P is the probability distribution of bond lengths, U_r is the bond potential as defined in Equation (3), k_B is the Boltzmann constant, and T is the absolute temperature. A similar approach is used for the bond angles and torsions. In order to correct for any error in the parameter calculation due to fitting a Boltzmann distribution to a condensed phase simulation, a coarse-grained MD simulation is run by using the parameter from the fit, and a new probability distribution is calculated. An updated Boltzmann distribution is fit to the existing distribution, generating another set of potential parameters. Parameters determined from both the atomistic and the coarse-grained simulations are used to calculate the final coarse-grained potential parameters as shown in Equations (20) and (21):

$$K_r^I = (K_r^{II})^2 / K_r^{III} \tag{20}$$

$$r_o^I = 2r_o^{II} - r_o^{III} \tag{21}$$

where I denotes the final coarse-grained parameter, II denotes a parameter determined from the atomistic simulation, and III denotes a parameter determined from the coarse-grained simulation. A similar approach can be applied to the bond angle and torsional potentials.

4.2.2 Molecular—meso-scale levels

Complementary hierarchical models have been developed very recently (Pearson *et al.*, 2009) that use MD and finite-element methods to examine nanoscale friction. However, for most of the systems, a buffer simulation level between molecular and meso-scale has rarely been investigated for the system containing complicated dynamics. However, this is a critical and challenging issue for the complete multi-scale simulation up to the continuum/device levels, although LBM reduces the scale difference as a meso-continuum scale simulation tool. For the HDD, it has been found that functional PFPE anchored on the surface or the coiled conformation of oligomer shows polarity due to the high interaction of functional groups, which forms coupling between functional PFPEs. A SRS model, which is highly coarse-grained molecular model, was invented to simplify polymer molecules

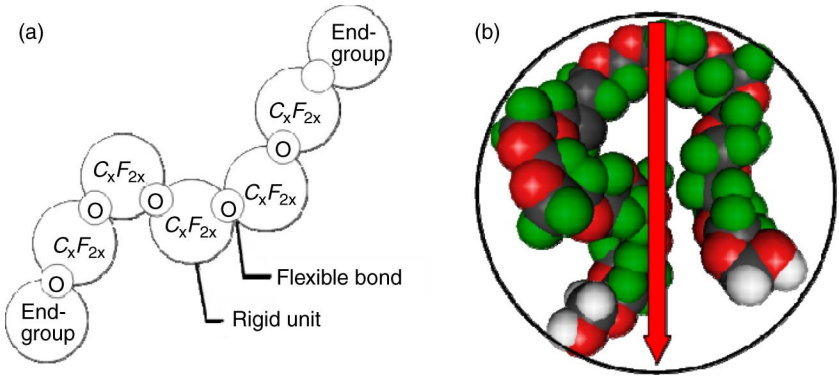

Figure 17 A sketch of the rigid units of an oligomeric PFPE molecule: (a) the flexible bonds with freely jointed beads and springs for coarse-grained bead-spring model and (b) SRS model with polarity (red arrow).

by considering the nature of coil conformation of polymer and polarity due to the functional groups. The SRS model describes the polymer chain with simple sphere with spins representing polarity (Figure 17). SRS was originally developed by Ma *et al*. (1999a) to simulate the spreading profiles of single component PFPE films over the carbon-overcoat via the MC. In the integration procedure of multi-scale modeling, the static properties (the spin orientation and radius of gyration of SRS, see Figure 18) from coarse-grained model can be estimated as SRS parameters. This implies that the SRS model can be systematically derived from *ab initio* via sequential coarse graining. SRS can be used as fundamental building block for constructing an LBM description for a lubricant/viscoelastic bearing.

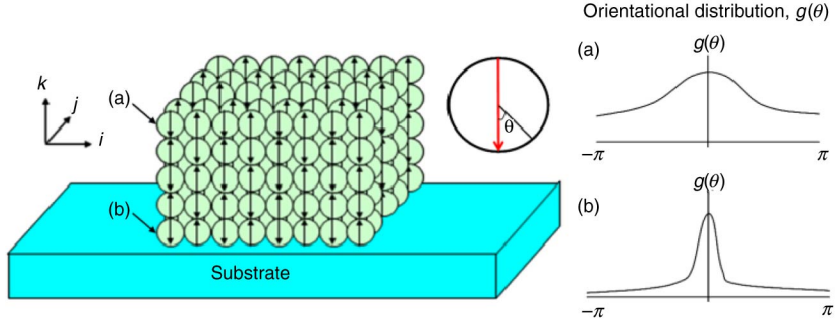

Figure 18 Generalized SRS model with orientational distribution $g(\theta)$ of molecules in (a) top and (b) bottom layers.

4.2.3 Meso-scale—continuum levels

For the integration of the multi-scale and multiphenomenological simulation, the strategy is to describe the entire system using LBM with parameters provided by lower level models. For the system with static geometry in equilibrium (e.g., PEFC), the geometric parameters can be accurately estimated via molecular-level simulation transferable to the continuum scale simulation. Wang *et al*. successfully simulated the continuum/device-level PEFC with direct numerical simulation techniques incorporating to a mesoscopic pore-scale description (Mukherjee and Wang, 2006, 2007; Wang *et al*., 2006b, 2006c, 2007), and Jain *et al*. (2010) expanded a continuum model to the molecular and system optimization scales via a middle-out approach to examine the effect of subsystems on the fuel cell performance. Systems with more complicated dynamics of subsystems (e.g., HDI) demand specific intermediate level of coarse-graining steps such as SRS. To devise LBM elucidating the behavior of the lubricant film, SRS, which is constructed using simplified information from MD via reactive coarse-grained particles, needs to be provided.

Since Boltzmann transport equation (BTE), which is derived to LBKE, is particle assumption-based theory, an SRS model can be implemented to BTE as follows:

$$\partial_t f_i^j + v\partial_s f_i^j + F\partial_v f_i^j = (f_i^{j,0} - f_i^j)/\tau \tag{22}$$

where s, v, i, 0, τ, and F are space, velocity, discrete directions, equilibrium state, relaxation time, and an external force, respectively. Superscript j denotes the orientation spin, which is statistically calculated from coarse-grained bead-spring model. The Ising model in ferromagnetism, the SRS model in lubricant theory, and a lattice gas are analogous mathematically (Jhon and Choi, 2001; Lee and Yang, 1952). At a lattice site, the Ising and SRS models simplify its spin as upward (↑) or downward (↓). Lattice gas considers that each lattice site is vacant (0) or occupied (1). Therefore, it is possible to construct a corresponding LBM model that can describe the mechanism drawn by spin interactions. The SRS model represents an oversimplified molecular picture but contains the essence of the molecule/surface interactions for describing molecular functionality (Karis *et al*., 2005). In the model, the spreading properties of lubricants are explained via spin characteristics, that is, $S = \pm 1$ (occupied sites) or $S = 0$ (vacant sites). In case of spreading of lubricants with polar endgroups, S^z (the projection of S in the direction perpendicular to the substrate, z) is used to identify the orientation of a polar endgroup ($S^z = \pm 1$, where a positive value denotes an upward-pointing endgroup) (Jhon and Choi, 2001). Only four

different interactions, molecule/molecule, molecule/surface, endgroup/endgroup, and endgroup/surface are considered for a simplified modeling. Thus, the Hamiltonian of this system may be written as

$$H = -\frac{J}{2}\sum_{i,j,k} S_{i,,j,k}S_{i\pm1,j\pm1,k\pm1} - A\sum_{i,j,k}\frac{S_{i,j,k}}{k^3} - K\sum_{i,j,k}\frac{1}{4}(S^z_{i,j,k}+1)(S^z_{i,j,k+1}-1) - W\sum_{i,j,k=1} S^z_{i,j,k} \tag{23}$$

where k is a counting index normal to the surface. The first two terms in the right-hand side represent interactions for nonreactive molecules (molecule/molecule interaction and molecule/surface interaction), implying that J is the nearest neighbor coupling constant, and A is related to the Hamaker constant originating from van der Waals interactions. The third and fourth terms represent characteristics of endgroup (descriptive for polar endgroup molecules only), where K and W represent the interaction between endgroups and the interaction between endgroups and the surface, respectively. Therefore, by setting $K = W = 0$, the Hamiltonian for nonreactive molecule systems is recovered for nonfunctional polymeric systems.

Using the Hamiltonian, we can obtain attractive or repulsive forces that play a role of external forces in Equation (22). A spin analogy/lattice gas model will be developed that can describe the oversimplified molecular structure, while still capturing the essence of the molecule/surface interaction. The relaxation time in SRS–LBM will contain shear rate and other nanoscopic information.

5. TECHNOLOGICAL APPLICATIONS: PEFC

This section deals with multi-scale models for the PEFC and consists of three subsections, 4.1, 4.2, and 4.3, that relate to molecular-level models, bridging models between scales and device/process level models, respectively. The objectives of these subsections are to survey the development and application of these models.

5.1 PEM

The PEM generally consists of polytetrafluoroethylene chains with hydrophilic perfluorosulfonate side groups. Water molecules within the system agglomerate in the vicinity of hydrophilic groups (i.e., sulfonic acid groups) and form hydrophilic clusters. A network of these clusters forms passages for proton conduction within PEM, which is

critical to PEFC performance. Hence a detailed relationship between PEM structure, water uptake, and proton conduction is necessary for synthesis of novel membrane materials, which overcome the limitations of state-of-the-art PEMs. *Ab initio* models of PEM have been studied to explain the first-principle dynamics of proton conduction mechanism in hydrated PEM (Choe *et al*., 2010; Habenicht *et al*., 2010). Quantum mechanical calculations are incorporated to atomistic MD simulations by providing accurate potential energy functions as inputs to MD simulations. The atomistic MD exhibits the correspondence to the experimental data as well as provides PEM structural information and proton transfer mechanisms in PEM (Jinnouchi and Okazaki, 2003). Komarov *et al*. (2010) utilized particle-based and field-based simulation techniques (i.e., integration of atomistic MD and dynamic DFT) to investigate the processes of self-organization in the systems of sulfonated poly(ether ether ketone)s in the presence of water. Goddard *et al*. (2006) used similar overlapping simulation methodologies for the PEM as well as CL and successfully applied a reactive force field from quantum mechanical calculations to larger scale MD simulations retaining the accuracy. The molecular-level model can be also applied for different electrocatalyst materials to determine atomistic or molecular mechanisms for electrochemical reactions and degradation of electrode. Franco and Gerard (2007, 2008) and Franco *et al*. (2009) analyzed degradation mechanisms of cathode CL in PEFC by using multi-scale mechanistic models.

Atomistic MD models can be extended to the coarse-grained level introduced in the previous section, which is determined by the dimension of the backbone chain and branch. For the precise description of water molecular behavior, simple point charge (SPC) model was adopted (Krishnan *et al*., 2001), which can be used to simulate complex composition systems and quantitatively express vibrational spectra of water molecules in vapor, liquid, and solid states. The six-parameter ($D_{\mathrm{OH}}, \alpha, \beta, L_{\gamma\theta}, L_{\gamma\gamma}$, and $L_{\theta\theta}$) SPC potential used for the water molecules is shown in Equation (24):

$$\begin{aligned} U_{123} = {} & D_{OH}[(1-\exp[-\alpha\, r_{12}])^2 + (1-\exp[-\alpha\, r_{13}])^2] \\ & + \left[L_{rr}\, r_{12}\, r_{13} + L_{\gamma\theta}(r_{12}+r_{13})r_{23} + \frac{L_{\theta\theta}(r_{23})^2}{2}\right] \\ & \exp\{-\beta[(r_{12})^2 + (r_{13})^2]\} \text{ with } r_{ij} = r_{ij} - r_{e,ij}, \end{aligned} \tag{24}$$

where $r_{e,ij}$ is the equilibrium distance between the ith and jth atoms. The subscripts 1, 2, and 3 correspond to the oxygen and the two hydrogen atoms, respectively. The water uptake in the electrolyte was examined

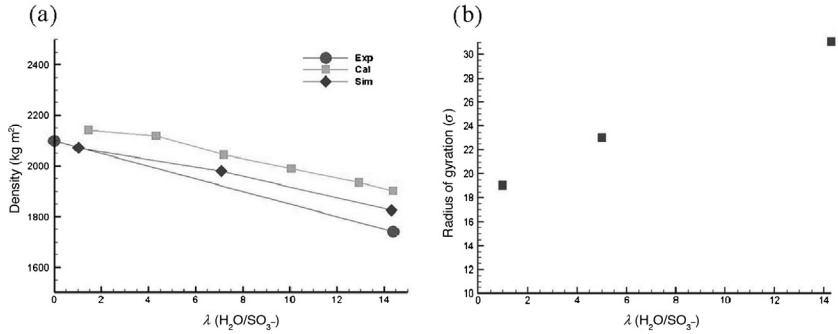

Figure 19 (a) Density of electrolyte (circle: experiment by Gierke et al. (1981), square: calculation by Jinnouchi and Okazaki (2003), diamond: our model) and (b) water uptake dependence of radius of gyration of Nafion® molecules.

from 1 to 14.3 H_2O/SO_3^-. Note that the electrolyte in the state of water uptake at 14.3 H_2O/SO_3^- is almost identical to the immersed proton form in this simulation.

One of the most important phenomena related to the electrolyte structure is water uptake variation in the PEM. The electrolyte swells upon water uptake, and the density of the electrolyte decreases in a humidified atmosphere. Swelling deformation has been considered as forming transport paths for the cluster of water molecules and protons. We first calculated the density of the PEM system for various amounts of water uptake. The squares and diamonds in Figure 19a indicate the experimental and simulated density for the dry and hydrated proton form of electrolyte (Gierke *et al*., 1981; Jinnouchi and Okazaki, 2003). As water content increases, the PEM density decreases in the simulations as well as experiments, and predicted values are in good agreement with experimental values, indicating that swelling phenomena of the electrolyte can be captured through this simulation. This swelling phenomena of Nafion® molecules is also illustrated via Figure 19b, which shows that the radius of gyration among the simulation species increases when the number of water molecules in the system increases. This indicates that as the area occupied by water molecules around the end of the side-chain increases, the Nafion® molecules tend to stretch-out geometrically. Haubold *et al*. (2001) found that side-chain unfolding of the polymer can be observed when the water content increases. In this simulation, we observed that increase in clustered regions of water not only affects the side-chain conformations but also the conformation of the backbone chain, making the polymer backbone chain stretched.

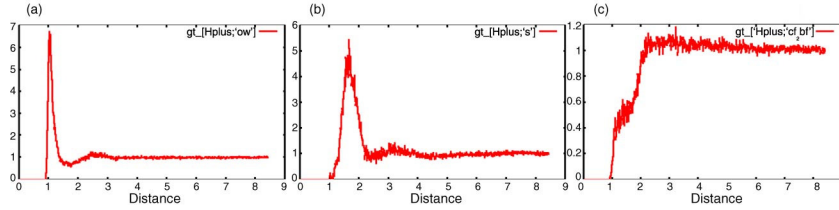

Figure 20 Radial distribution function: (a) H^+–H_2O, (b) H^+–S, (c) H^+–CF_2.

The evidence of water–water cluster generation in the wet electrolyte has been provided through several experimental techniques such as small-angle X-ray scattering, transmission electron microscopy, and Fourier transform infrared spectroscopy (FTIR) (Falk, 1980; Porat *et al*., 1995; Roche *et al*., 1981). It has been reported that polar particles (water and protons) cohere in the electrolyte. We also confirmed such phenomena in this simulation via radial distribution functions (RDFs) among the species (Figure 20). The sharp peak in RDFs between polar species indicates that almost all the protons and the water molecules always exist within the clustered region. However, we did not observe significant peaks between the polar and nonpolar particles. These results indicate that polar particles cohered in our simulations as well. Figure 21 illustrates the two-dimensional snapshot of water density distribution within the simulation cell for various amounts of water content (H_2O/SO_3^-). It is clearly observed that the high water density region increases as the water content increases. This high water density region corresponds to the clusters observed in previous experimental studies. The increase of the high water density region implies an increase of the number of the transport paths for polar particles. The alignment of these clusters is disorderly, and highly tortuous transport pathways are constructed in our electrolyte model.

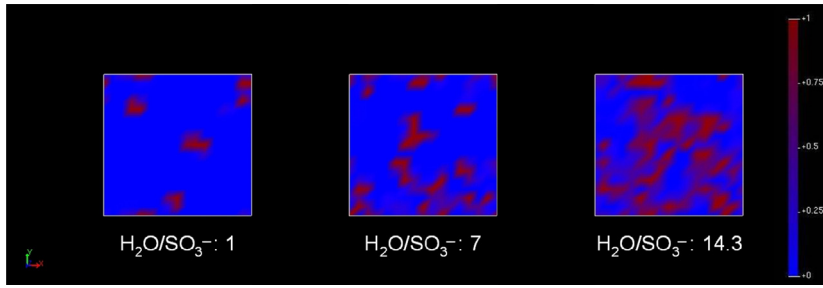

Figure 21 Water density distributions in a cross section of the system.

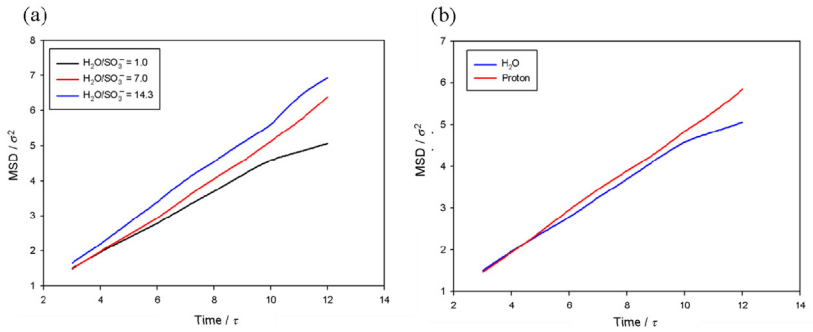

Figure 22 (a) Water content dependence of mean square displacement (MSD) of protons and (b) MSD of protons and water molecules (H_2O/SO_3^-: 1).

Researchers have shown that protons and water molecules move together through the clusters constructed in electrolytes. Although several theoretical methods using macroscopic modeling have been proposed based on the information of the electrolyte structure, there is no model that estimates transport properties from the subcontinuum modeling viewpoint. From Figure 22a, we observe that the MSD of protons increases as the water content increases. In other words, the diffusivity of the protons (proportional to the gradient of MSD) increases as the water content increases. Thus, the diffusion of protons in the PEM depends on the water content. This phenomenon can be explained in terms of the electrolyte structure. As discussed before, the water molecules and ions cohere with each other and construct hydrophilic clusters in a humidified electrolyte. These clusters join with each other and form transport pathways for the protons and water molecules. Evidence that the protons and water molecules move through this cluster region has been obtained from the RDF. Hence, we can conclude that the cluster region is the transport path for protons and water molecules. The shape parameters of the clustered region, such as the cluster size and clusters connectivity, can strongly affect the transport properties in the electrolyte. The low diffusivity in the electrolyte is due to the tortuous shape of the cluster region. The ions and water molecules in an electrolyte solution can move freely in all directions, but particles in the PEM cannot, due to the tortuous hydrophobic wall. Figure 22b illustrates the comparison between diffusivity of water molecules and protons. We observe that the diffusion coefficient of the protons is smaller than that of the water molecule, and the activation energy of protons is higher than that of water molecule. This indicates that the resistance to transport of protons is higher than the water molecules.

5.2 Multiphenomena in gas diffusion layer

An entire PEFC model has been successfully investigated via continuum mechanics (Mukherjee and Wang, 2006, 2007; Rama *et al*., 2010; Wang *et al*., 2006b, 2006c, 2007), which does not contain detailed molecular structural information or simulate complex multiphase, multiphysical phenomena. In addition, conventional continuum mechanics has limitations to simulate the complex two-phase gas–liquid flow phenomena within the porous GDL. To overcome this issue, LBMs can be introduced. This method is specifically useful for simulating multiphase flows as well as hybridizing molecular with continuum level theories (Hao and Cheng, 2010; Sukop *et al*., 2008; Yu and Fan, 2010). Since the LBM covers from meso-scale to continuum levels, it is straightforward to combine GDL (meso-scale/continuum level) and GC (continuum level).

For the porous media flow simulation, LBM can be applied on the complex geometry of porous media due to its advantages on handling such geometry. However, in spite of this convenience, the calculation cost will be drastically increased as the system size increases up to the device level approximately in millimeter scale and above. To develop larger scale buffer simulation, representative elementary volume (REV) method was invented, where single lattice represents the volume of porous media. The fuel flowing in the porous electrode can be described by a continuity equation and the Brinkman–Forchheimer–extended Darcy equations (generalized momentum equation) (Nithiarasu *et al*., 1997):

$$\nabla \cdot \mathbf{v} = 0 \tag{25}$$

$$\frac{\partial \mathbf{v}}{\partial t} + (\mathbf{v} \cdot \nabla)\left(\frac{\mathbf{v}}{\phi}\right) = -\frac{1}{\rho}\nabla(\phi P) + \mathbf{v}\nabla^2\mathbf{v} + \mathbf{F} \tag{26}$$

where ϕ is the porosity, P is the cell total pressure, and $\mathbf{v}$ is the kinematic viscosity. $\mathbf{F}$ represents total body force due to the presence of the porous medium and other external force fields, expressed by

$$\mathbf{F} = -\frac{\phi \mathbf{v}}{K}\mathbf{v} - \frac{\phi F_\phi}{\sqrt{K}}|\mathbf{v}|\mathbf{v} + \phi G \tag{27}$$

where G is the body force induced by an external force, and F_ϕ and K are, respectively, the geometric function and permeability, which can be estimated from Ergun's experimental results and expressed by (Ergun, 1952; Vafai, 1984)

$$F_\phi = \frac{1.75}{\sqrt{150\phi^3}} \quad \textit{and} \quad K = \frac{\phi^3 d_p^2}{150(1-\phi)^2} \tag{28}$$

where d_p is the effective average diameter of the solid in the porous electrode.

Generally, the BTE with single relaxation time approximation can be written as Equation (15). In order to simulate flow in the porous media, we consider the drag effect of the medium and present the LBM equation by the following form of the statistical average:

$$\bar{f}_i(\mathbf{x} + \mathbf{c}_i t, t + t) = \bar{f}_i(\mathbf{x}, t) - \frac{1}{\tau}[\bar{f}_i(\mathbf{x}, t) - \bar{f}_i^{eq}(\mathbf{x}, t)] + F_i t \tag{29}$$

where $\bar{f}_i(\mathbf{x}, t)$ and $\bar{f}_i^{eq}(\mathbf{x}, t)$ are volume-averaged distribution function and equilibrium distribution function at REV scale, respectively (from now on, the overbars will be omitted for the sake of convenience). F_i is the force term for ith particle of fluid. According to Cancelliere *et al*. (1990), F_i is chosen as

$$F_i = \omega_i \rho \left(1 - \frac{1}{2\tau}\right)\left(\frac{\mathbf{e}_i \cdot \mathbf{F}}{c^2} + \frac{(\mathbf{e}_i \cdot \mathbf{v})(\mathbf{e}_i \cdot \mathbf{F})}{\phi c^4} - \frac{\mathbf{v} \cdot \mathbf{F}}{\phi c^2}\right) \tag{30}$$

The density and velocity of the fluid are defined by

$$\rho(\mathbf{x}, t) = \sum_i f_i \quad \textit{and} \quad \mathbf{v}(\mathbf{x}, t) = \frac{1}{\rho(\mathbf{x}, t)} \sum_i \mathbf{c}_i f_i + \frac{t}{2}\mathbf{F} \tag{31}$$

The macroscopic equations for fluid flowing in porous media may be recovered by Taylor expansion and Chapman–Enskog expansion, which become

$$\frac{\partial \rho}{\partial t} + \nabla \cdot (\rho \mathbf{v}) = 0 \tag{32}$$

$$\frac{\partial(\rho \mathbf{v})}{\partial t} + \nabla \cdot \left(\frac{\rho \mathbf{v}\mathbf{v}}{\phi}\right) = -\nabla P + \nabla \cdot [\rho \mathbf{v}(\nabla \mathbf{v} + \mathbf{v}\nabla)] + \mathbf{F} \tag{33}$$

We see that above equations recover Equations (25) and (26) for $\rho =$ constant. Note that as $\phi = 1$, Equation (26) or (33) is reduced to the standard LBKE for the fluid flows in the absence of porous media.

Xu *et al*. (2006b) have successfully introduced Brinkman–Forchheimer–extended Darcy equation in order to solve the performance of molten carbonate fuel cell. As a verification of REV method, Poiseuille flow profiles in the porous media modifying LBM with

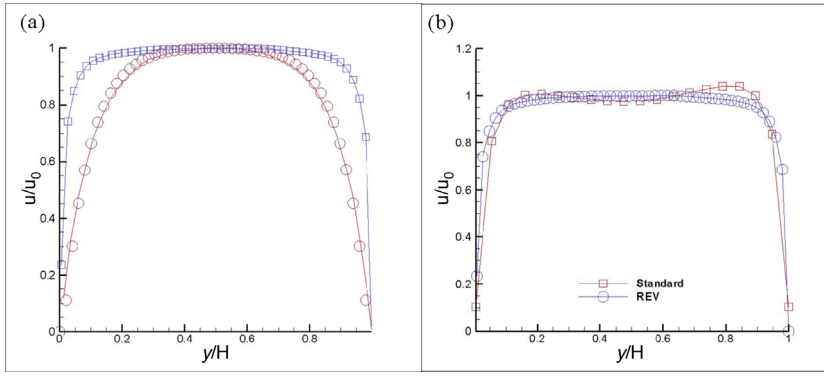

Figure 23 (a) Comparison of normalized velocity profile (Re = 0.1); solid line: analytical solution, symbol: LBM; blue: Da = 10^{-4}, red: Da = 10^{-3}, $\phi = 0.1$ and (b) comparison of REV (blue) and standard (red) methods: Re = 0.1, Da = 10^{-4}, $\phi = 0.1$.

Brinkman–Forchheimer–extended Darcy equation were simulated. The porosity is set to be 0.1, Reynolds number (Re) changes from 0.01 to 100, and the Darcy number (Da) changes from 10^{-6} to 10^{2}. The lattice used is an 80×80 square mesh, and the relaxation time is set to be 0.8. Periodic boundary conditions are applied to the entrance and the exit. The velocity field is initialized to be zero at each lattice node with a constant density $\rho = 1.0$, and the distribution function is set to be its equilibrium at $t = 0$. In Figure 23a, the numerical results of the REV LBM are compared with the finite difference results, which were solved by Guo and Zhao (2002). Excellent agreement is observed between REV LBM and the finite-difference solutions, which confirms the validity of the REV LBM for the continuum scale exhibiting that velocity profiles tend to be the same when the finer porous media is used with same porosity. REV LBM is also compared to the standard LBM with manipulated porous media geometry having same parameter conditions as a verification in lower scale level. Figure 23b shows that the standard LBM with porous geometry shows the behavior similar to the results from REV LBM. Since the flows in PEFC have multicomponent/multiphase characteristics, which result in clogging effects, the details of porous media geometry cannot be discarded for an accurate GDL model. Therefore, multi-scale integration in GDL can be obtained via combining REV LBM and LBM with the porous media geometry.

LBKE can be further modified to capture the multicomponent/multiphase phenomena in GDL as well as GC. This modification also allows modeling the hydrophilic effect such as the bubble transport phenomenon. Lu and Wang visualized the bubble phenomenon in situ using the

hydrophilic carbon cloth since it has more regularly distributed pores than the hydrophobic one. Therefore, the hydrophilic diffusion layer is more preferred to remove bubbles. In order to simulate a multicomponent, multiphase flow in the fuel cell, we need to solve the same number of LBKEs as the number of components. The additional effects from the multiphase flow, such as the surface tension, the fluid–solid force, and the buoyancy force can be treated as external forces for the momentum equation. Therefore, modified LBM equation can be expressed as

$$\rho^{\sigma}(x,t)v^{\sigma}(x,t) = \sum_{i} f_i^{\sigma}(x_i,t)c_i + F^{\sigma}_{total}(x,t) \tag{34}$$

as the general momentum equation for the multicomponent, multiphase flow. In Equation (34), $F^{\sigma}_{total}(x,t)$ represents the total external force parameter (momentum per volume) of the component σ (species) contributed by the surface tension, the fluid–solid interaction force, and the buoyancy force

$$F^{\sigma}_{total}(x,t) = F^{\sigma}_{surface\ tension}(x,t) + F^{\sigma}_{fluid-\sigma o\lambda\iota\delta}(x,t) + F^{\sigma}_{buoyancy}(x,t). \tag{35}$$

In order to model the surface tension force in the multicomponent fluid, an interaction potential $\phi(x, x')$ was defined. This potential can be represented by

$$\phi(x,x') = G^{\sigma\sigma'}\psi^{\sigma}(x)\psi^{\sigma'}(x'). \tag{36}$$

where $\psi^{\sigma}(x)$ is a function of the mass density of the species σ at the position vector $\mathbf{x}$; and $G^{\sigma\sigma'}$ is set to be the interaction strength between the species σ and the other species σ'. For simplicity, we assume that $G^{\sigma\sigma'}$ only accounts for the nearest-neighbor interactions. The rate of change of the momentum per volume for the multicomponent fluid then becomes

$$\frac{dF^{\sigma}_{surface\ tension}}{dt}(x,t) = -\Psi^{\sigma}(x,t)\sum_{\sigma'} G^{\sigma\sigma'}\sum_{i}\Psi^{\sigma'}(x+e_i\,t,t)e_i. \tag{37}$$

Hence, the force parameter contributed by the surface tension can be approximated by the following equation:

$$F^{\sigma}_{surface\ tension}(x,t) = -\tau^{\sigma}[\Psi^{\sigma}(x,t)\sum_{\sigma'} G^{\sigma\sigma'}\sum_{i}\Psi^{\sigma'}(x+e_i\,t,t)e_i] \tag{38}$$

where τ^{σ} is the collision time for the species σ.

The interaction force at the fluid–solid interaction can be expressed by

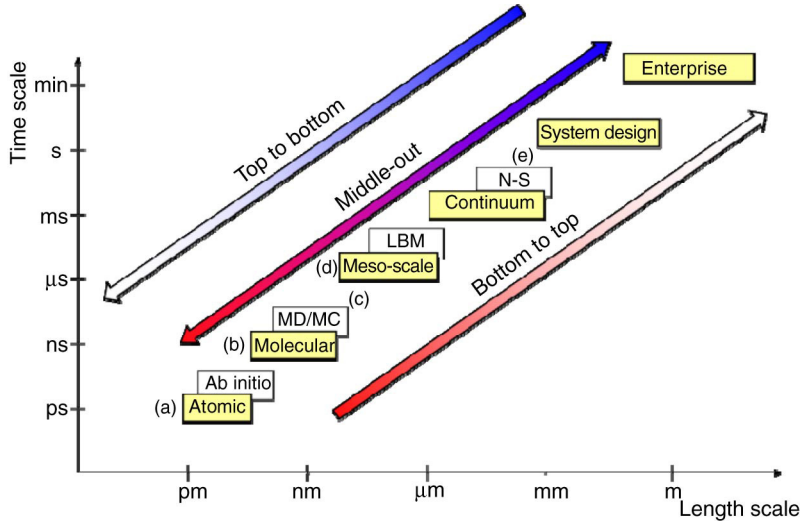

Figure 24 Multi-scale/holistic interpretation of physical system.

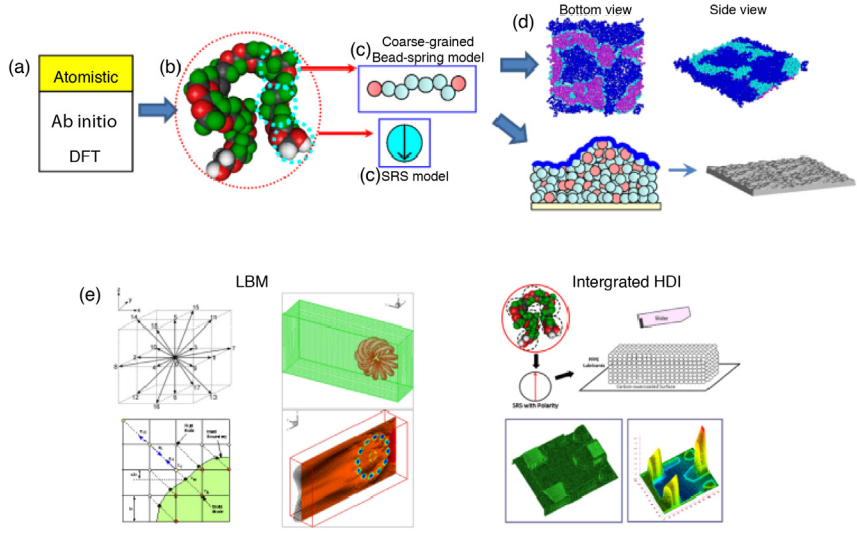

Figure 25 Multi-scale modeling of HDI: (a) *ab initio* (atomic), (b) MC/MD (molecular), (c) coarse-graining procedure (molecular/meso-scale), (d) diffusion characteristics and surface topography, and (e) LBM (meso-scale) and integration HDI (system design).

$$F^{\sigma}_{fluid-solid}(x,t) = -\rho^{\sigma}\sum_{i} G^{\sigma}_{i}s(x+e_i\,t)e_i \tag{39}$$

where G^{σ} is the fluid–solid interaction potential parameter; s is a function of the position of the particle, $s=0$ when the particle is in the fluid, and $s=1$ when the particle is at the fluid/solid interface. The angle between the fluid and the wall, due to the hydrophilicity, can be controlled by adjusting the fluid–solid interaction potential parameter G^{σ}. The angle increases with larger G^{σ}. When the contact angle increases, the wall is less hydrophilic. The momentum contributed by the buoyancy force can be expressed by the following equation:

$$F^{\sigma}_{buoyancy}(x,t) = -g\sum_{i} \rho^{\sigma}(x+e_i\,t,t)e_i \tag{40}$$

where g is the gravitational constant.

5.3 Device-scale/process-scale level

A more physically accurate representation includes space–time dependencies on physical parameters via conservation laws as well as electrochemistry based on irreversible thermodynamics. As shown in Figure 4, the model for PEFC system consists of an integrated assembly of several interacting physical components, each comprising of multidimensional, multiphysical transport and electrochemical reaction processes. There are seven chambers in the model, the GCs, the GDLs, and the CLs both on anode and the cathode sides, and a central PEM region. This device-level model is based on multiphase continuum mechanics coupled with species, and energy conservation along with electrochemistry. The equations descriptive for various subcomponents are integrated and incorporated into the optimization framework. Although this approach primarily originated from continuum mechanics, one can obtain spatial dependencies and temporal resolution of physical parameters through an optimization scheme, which contains design criteria one level deeper. This multi-scale approach was applied to obtain an optimal CL design with spatial variation of the CL layer and platinum loading (Jain *et al.*, 2008). Further work demonstrated the sensitivity of this design for refining these PEFC models (Jain *et al.*, 2010).

At the process level, efficient flowsheet optimization strategies based on lumped parameter models are now widely used in practice (Biegler *et al.*, 1997). At this scale, the PEFC is embedded within a power plant flowsheet model, as shown in Figure 3. The process comprises

three subsystems (1) the fuel processing, (2) the PEFC stack, and (3) the postcombustion (Xu *et al*., 2006a). The design questions at this level are addressed through optimization of network connections of these subsystems, the heat exchanger network, as well as equipment design of individual components (PEFC, reactors, compressors) within each subsystem. As considered in Xu *et al*., the flowsheet is designed to maximize power for a given feed and an equilibrium model is used for the PEFC. While this model neither handle the spatial characteristics of device-level PEFC models nor the design of the membrane material, the process-scale model can be replaced by a ROM to handle these features. By applying the ROM-based optimization strategy developed in Lang *et al*. (2009, 2011), information from device- and molecular-scale models can be used to construct the ROM in order to include decisions that relate to material and device-level performance.

6. TECHNOLOGICAL APPLICATIONS: HARD DISK DRIVE

As emphasized in the previous section, it is critical for the multi-scale integration to develop mathematically simple (with few parameters) yet physically realistic models with nanoscopic information. For the description of the multi-scale framework of HDI, we provide a bottom-up approach as given below to sketch multi-scale modeling as described in Figures 24 and 25 (Jhon *et al*., 2011).

Perform atomistic simulations to obtain force field parameters to be used in step 2 (Figures 24a and 25a). In this step, *ab initio* methods and/or DFT are utilized to calculate the intramolecular force field parameters (stretching, bending, and torsional) from the Hessian matrix (Smith *et al*., 2011). The potential energy among PFPE molecules and PFPE–carbon surface interactions are also calculated as a function of the endgroup structure (e.g., Zdol and Ztetraol) via parameter estimation for the given potential energy functional form. This information is used for MD simulation in step 2.

Employ classical MD to calculate mesoscopic properties of molecularly thin lubricant films from the atomistic input obtained from step 1 (Figures 24b and 25b). During the past decade, atomistic/coarse-grained MD models for PFPE systems based on Langevin equations have been investigated (Chung *et al*., 2009; Guo *et al*., 2006; Ma *et al*., 1999a, 1999c; Phillips and Jhon, 2002). Step 1 will provide additional input to these models by delivering first-principle information as well as numerical accuracy.

Further employment of the coarse-graining process to represent PFPE molecules with few parameter models (having the least

parameters yet preserving essence of physics) such as size, shape, and orientation of endgroups (simplest example is SRS (Figures 24c and 25c) where the shape is spherical and orientation is spin-like quantized form).

Develop an LBM scheme with generalized SRS model to accurately describe the dynamics of PFPE systems. The model is based on the mathematically simple yet physically realistic LBM models capturing the bottom level (atomistic) information. This novel formulation is based on our system for electron–phonon coupling with two states (Ghai *et al.*, 2005), which is analogous to spin system description for endgroups.

Couple LBM to be developed in step 4 with LBM schemes descriptive for air bearing and thermal phenomena (Figures 24e and 25e).

From the mesoscopic model described in steps 2 and/or 3, calculate physical properties including spreading, surface energy, diffusion processes, and compare the simulation results with experimental data. This can be done for pure and nanoblended PFPE systems (Figures 24d and 25d).

Design the advanced HDD from our multi-scale simulation tools described in steps 4 and 5. Integration of HDI simulation stated in steps 1–6, can be easily achieved via a slight extension of our current understanding, although at the current stage we are not employing systematic parameter estimation techniques yet by introducing sophisticated optimization tools. Furthermore, the techniques like reduced-order methods may be useful in reducing the degrees of freedom systematically. This methodology will be useful in our future HDD development.

6.1 The coarse-grained, bead-spring model

Molecular simulations via the coarse-grained, bead-spring model were carried out to examine the nanostructure of PFPE lubricant films, including the anisotropic radius of gyration and endbead density profile (Izumisawa and Jhon, 2002a, 2002b; Jhon *et al.*, 2003). Guo *et al.* (2004, 2005) pioneered MD simulation to investigate both static and dynamic properties of PFPE films to explain the underlying physics in the experimental findings of PFPE films as well as develop a powerful numerical tool to understand the properties of PFPE films at molecular level. The atomic or united atom models are mainly adopted for the simulation of simple particles or short chains, while the coarse-grained, bead-spring model is suitable to simulate the polymeric system with a larger length scale. With the advantage of reduced computational cost, the coarse-grained, bead-spring model has been widely adopted to simulate the behaviors of polymeric systems (Milchev and Binder, 1996; Milchev *et al.*, 1993; Sheng *et al.*, 1994). Since PFPE and its derivatives

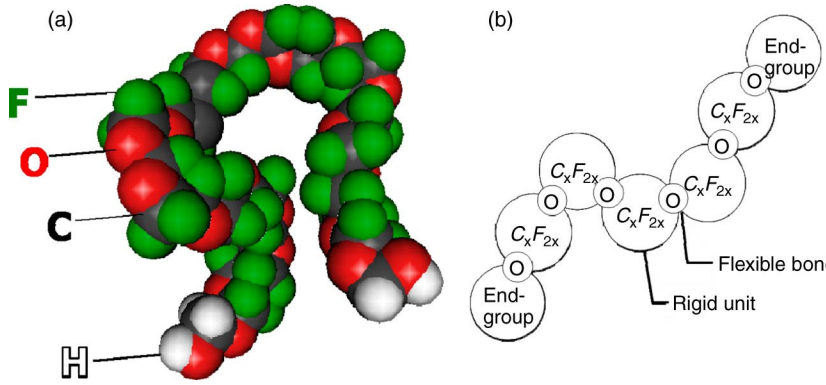

Figure 26 (a) A molecular model of an oligomeric PFPE Zdol molecule with $p = q = 10$ and $M_n = 1974$ g/mol and (b) simplification of the rigid units of an oligomeric PFPE molecule and the flexible bonds with freely jointed beads and springs.

have relatively high molecular weights, Jhon *et al*. adopted the coarse-grained, bead-spring model thereby simplifying the detailed atomistic information while preserving the essence of the internal molecular structure to examine static and dynamic properties of PFPEs (Guo *et al*., 2003; Izumisawa and Jhon, 2002a, 2002b). In the coarse-grained, bead-spring model, PFPEs are characterized by a sequence of freely joined rigid beads as shown in Figure 26.

In the HDI system, the root mean square (RMS) roughness of the carbon-overcoat surface, which corresponds to the solid surface, has been reduced to 2.3 (Fung *et al*., 2000). Therefore, it is reasonable to assume a perfectly flat and structureless wall on the bottom of the simulation cell for the system with coarse-grained, bead-spring model. This assumption has been justified via the spreading profiles of PFPE Zdol on the silica surface (molecularly smooth) (O'Connor *et al*., 1996) similar to those on the carbon surface (molecularly rough) (Ma *et al*., 1999b, 1999c, 1999d). The van der Waals interaction between bead and the surface $U_{VDW}(z)$ is then calculated by

$$U_{VDW}(z) = \varepsilon_w \left[\frac{1}{2} \left(\frac{\sigma}{z} \right)^9 - \frac{3}{2} \left(\frac{\sigma}{z} \right)^3 \right]. \tag{41}$$

Here, z is the distance from the surface and ε_w is the potential depth of the bead and surface interaction. Due to the repulsive contribution in Equation (41), beads are prevented from moving very close toward the solid surface. Figure 27 illustrates a schematic of the coarse-grained, bead-spring PFPEs with the flat surface assumption. The functional

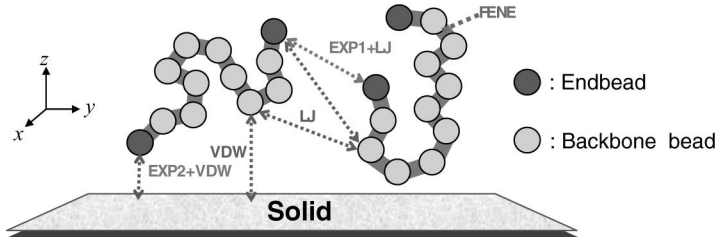

Figure 27 A schematic of coarse-grained, bead-spring model with potential energies (PFPE).

beads in PFPE interact much differently from LJ or dispersive type interactions; however the mechanism has not yet been clarified, which could be hydrogen bonding, hydrogen transfer, or esterification. To maintain the generality and demonstrate potential energy characteristics of a short-range interaction without losing the essence of the chain-end related problem, such as that found in functional PFPE films, short-range exponential (EXP) decay functions in addition to dispersive interaction (i.e., U_{LJ} and U_{VDW}) are used between functional beads, $U_{\mathrm{EXP1}}(r_{\mathrm{ee}})$, as well as between the functional bead and the surface, $U_{\mathrm{EXP2}}(z)$ as illustrated by Equations (42) and (43). Specifically, for the interaction between endbeads, $U_{\mathrm{eb-eb}} = U_{\mathrm{LJ}} + U_{\mathrm{EXP1}}$; and for the interaction between endbeads and surface, $U_{\mathrm{eb\text{-}surface}} = U_{\mathrm{VDW}} + U_{\mathrm{EXP2}}$. Due to the strong short-range interaction in the decay functions, functional endgroups prefer to couple with the solid surface rather than backbone chains, as long as they are close enough to the bottom surface. Here,

$$U_{EXP1}(r_{ee}) = -\varepsilon_b^p \exp\left(-\frac{r_{ee} - r_c}{d}\right), \tag{42}$$

and

$$U_{EXP2}(z) = -\varepsilon_w^p \exp\left(-\frac{z - z_c}{d}\right). \tag{43}$$

where, r_{ee} denotes the distance between endbeads and d is the characteristic decay length for the short-range interaction and ε_b^p and ε_w^p are the potential depths at $r_{\mathrm{ee}} = r_{\mathrm{c}}$ and $z = z_{\mathrm{c}}$. A larger value of ε_b^p indicates a stronger endgroup functionality.

Endbead density profiles for functional and nonfunctional PFPEs were examined by Guo *et al*. (2003). Figure 28a shows the endbead density profiles of single component PFPEs as a function of the bead and surface interaction strength ε_{w} in Equation (41) and endgroup functionality $\varepsilon_{\mathrm{b}}^p$ and $\varepsilon_{\mathrm{w}}^p$ in Equations (42) and (43). For nonfunctional

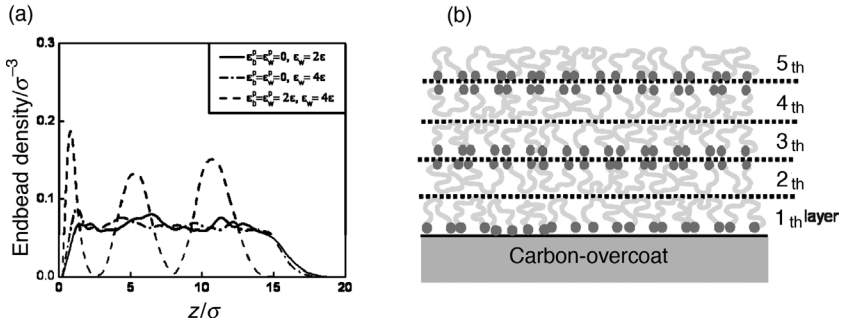

Figure 28 (a) The endbead density profiles of PFPE nanofilms as a function of ε_w, ε_b^p, and ε_w^p with $N_p = 10$ and $T = 1.0\varepsilon/k_B$ by Guo et al. and (b) a schematic of the "layering" structure for functional PFPE nanofilms.

PFPEs $\left(\varepsilon_b^p = \varepsilon_w^p = 0\right)$, the endbeads are uniformly distributed through the entire film thickness (z). Slightly intensive adsorption on the surface was also observed for a stronger surface attraction ($\varepsilon_w = 4\varepsilon$), which shows the surface interaction strength is negligible for the film conformation of nonfunctional PFPEs as well as backbone of functional PFPEs. For functional PFPE $\left(\varepsilon_b^p = \varepsilon_w^p = 2\varepsilon\right)$, the endbead density is maximized near the bottom surface with $\sigma = 1$. Oscillation of the endbead density profile occurs for functional PFPEs, originating from the endbead–endbead couplings. We also notice that the distance between two neighboring peaks in Figure 28a is about 5.5σ, which corresponds to the thickness of two layers (Guo *et al.*, 2003). Therefore, this result verifies that the coarse-grained, bead-spring model qualitatively describes the endgroup coupling between functional PFPE molecules as well as the layering structure in the functional PFPE film. This is ideally described in Figure 28b, where the functional PFPEs tend to anchor with endgroups onto the surface in the first layer and form the subsequent layers with coupled endgroups.

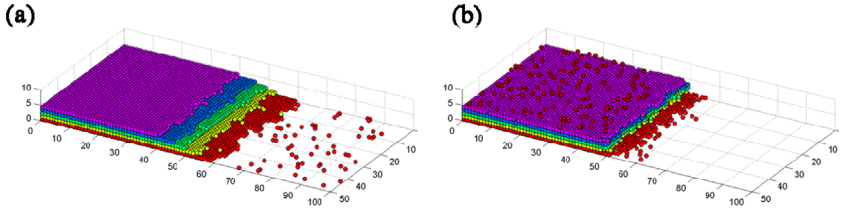

Figure 29 Spreading profile of SRS models with (a) nonfunctional and (b) functional PFPEs by Ma et al.

6.2 Simple reactive sphere model

SRS with spins representing the endgroup orientation was first proposed by Ma *et al*. (1999a) to simulate the spreading profiles of single component PFPE films over the carbon-overcoat via the MC method (Figure 29). This work was later extended to simulate the spreading profiles of single component PFPE films over hydrogenated and nitrogenated carbon-overcoats (Phillips *et al*., 2001; Vinay *et al*., 2000) as well as their surface characteristics (Phillips and Jhon, 2002). However, the SRS model does not capture the detailed structure of PFPE molecules. Therefore, in order to utilize SRS to understand the geometry of submonolayer lubricant films, as well as investigate the molecular conformation and the resultant static and dynamic properties of PFPE films, it is necessary to incorporate intramolecular degrees of freedom from high-resolution scale models such as coarse-grained, bead-spring or atomistic models.

Due to the van der Waals interaction between backbone bead and carbon-overcoated surface, PFPE has an oblate rather than spherical conformation. So the current SRS model should be modified by allowing position dependent deformations. To analyze molecular structures in the nanofilm, the molecular conformation of coarse-grained, bead-spring PFPEs on the surface is defined with the radius of gyration (R_g), including the parallel ($R_{||}$) and perpendicular ($R_{\perp}$) components (Guo *et al*., 2003), corresponding to the radius of gyration in the direction parallel and perpendicular to the bottom surface (Figure 30):

$$R_{||}^2 = \frac{1}{2N_p}\sum_{i=1}^{N_p}[(x_i - x_g)^2 + (y_i - y_g)^2],$$
$$R^2 = \frac{1}{N_p}\sum_{i=1}^{N_p}(z_i - z_g)^2 \quad \textit{with } R_g^2 = R^2 + 2R_{||}^2 \tag{44}$$

Here, N_p is the total number of beads in each PFPE molecule, (x_g, y_g, z_g) are the coordinates of the PFPE molecular center of mass, and (x_i, y_i, z_i) denote the bead coordinates. The perpendicular size of PFPE

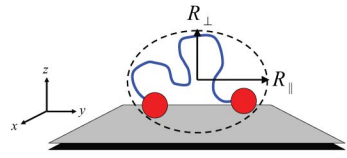

Figure 30 A schematic of the parallel and perpendicular radius of gyration of PFPE molecule on the surface.

especially controls the thickness of monolayer film. The radius of gyration can be considered as a SRS configuration parameter, which identifies the form of SRS model on the surface (e.g., oblate, spherical, or prolate conformation).

6.3 Meso-scale/continuum level

The air bearing of the HDI operates under rarefied gas flow, which is the high Knudsen number (*Kn*) flow regime. The conventional Navier–Stokes equations are not eligible to describe the flow inside the air bearing because the continuum hypothesis is no longer valid in the high *Kn* regime. Therefore, the modified Reynolds equation (MRE) has been constructed to solve high *Kn* flow of the air bearing (Fukui and Kaneko, 1987; Kang *et al*., 1999). Accurate velocity slip modeling on the wall is crucial for the high *Kn* flows and several slip models have been developed that incorporate the molecular rarefaction effect to describe the slip flow via two parameters, *Kn* and surface accommodation coefficient. Although the MRE is widely used for the slider design, it is not well suited to HDI integrated modeling, because it does not have flexibility and capability for integration of the multi-scale system including the air-bearing, lubricant film, and nanoscale heat transfer in media. Recently, Myong *et al*. (2005) developed the boundary model based on the theory of adsorption phenomena pioneered by Langmuir. According to Langmuir's theory, gas molecules do not reflect directly, but rather reside on the surface for a brief period of time due to the intermolecular forces between the gas molecules and the surface atoms. After some lag in time these molecules may reflect from the surface. This time lag causes macroscopic velocity slip. From this physical context, the fraction of surface covered at equilibrium for monatomic and diatomic gases is written respectively as

$$\alpha = \frac{\beta p}{1 + \beta p} \tag{45}$$

$$\alpha = \frac{\sqrt{\beta p}}{1 + \sqrt{\beta p}}. \tag{46}$$

It was shown that the parameter α is function of pressure p. β is the reaction constant for surface–gas molecules interaction and is defined as

$$\beta = \frac{A l_\lambda / Kn}{K_B T_w} \exp\left(\frac{D_e}{K_B T_w}\right), \tag{47}$$

where A, K_B, D_e, and l_λ are the mean area of a site, the Boltzmann constant, a potential energy parameter, and the molecular mean free path, respectively. The potential energy of heat adsorption D_e varies with the type of gas and the nature of the wall material. α is a function of the wall temperature T_w, and plays a role similar to the slip coefficient of the Maxwell model slip model. The slip velocity, u_s of the Langmuir slip model can be calculated by

$$u_s = \alpha u_w + (1 - \alpha) u_g, \tag{48}$$

In LBM, the slip velocity on the wall can be defined by applying streaming and bounce-back process. Typical bounce-back and slip condition on the wall in LBM can be expressed as

$$\begin{pmatrix} f_7 \\ f_4 \\ f_8 \end{pmatrix} = k \begin{pmatrix} f_5 \\ f_2 \\ f_6 \end{pmatrix}, \quad k = \begin{pmatrix} r & 0 & s \\ 0 & r+s & 0 \\ s & 0 & r \end{pmatrix}, \tag{49}$$

where two parameters, r and s represent the fraction of the distribution function to be bounced-back and slipped forward, respectively (Sbragaglia and Succi, 2005), and they should be chosen such that $r + s = 1$. The slip velocity on the wall can be defined by summation of the distribution in consideration with the direction. The difference of two functions along the wall $(f_1 - f_3)$ within the summation can be denoted as the moving wall momentum (ρu_w). Thus

$$\rho u_s = s \sum c_i f + r \rho u_{wi}. \tag{50}$$

Equation (50) physically has the same meaning as the Langmuir slip model when r is chosen as α. For the 3D case, the 5×5 matrix k can be easily built up by using r and s in the same manner as in 2D.

Kim *et al*. (2007) examined the normalized velocity profiles at various values of Kn. In Figure 31, the computation result using the Langmuir slip model exactly matches those of the Maxwell and Beskok's slip model (Beskok, 2001) at $Kn < 0.1$. For the cases of $Kn = 0.1$ and 1 velocity profiles are also presented in Figure 31 and the results are compared with those obtained from the first-order slip model flow, Hsia and Domoto (1983), and the Maxwell models. The result using the Langmuir slip model exactly matched the one from the first-order slip flow but showed a slight deviation with the result using the Maxwell slip model, which may be caused by the fact that the Maxwell slip model can be considered to be a subset of the Langmuir slip model in the microchannel flow analysis at $Kn < 0.1$ only. 2D flow induced by a moving plate (Couette flow) with $Kn = 0.1$ and 1 was also

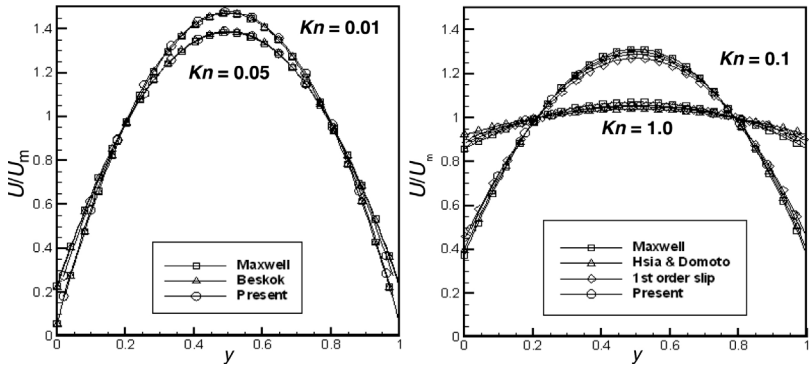

Figure 31 Normalized velocity distribution of Poiseuille flow at various Kn.

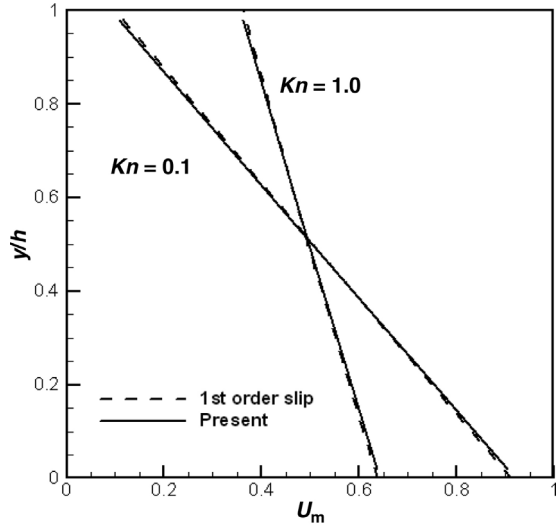

Figure 32 Normalized velocity distribution of Couette flow at various Kn.

simulated to verify the applicability of the slip model to air bearing simulation. The velocity comparisons with the first-order slip flow are shown in Figure 32. In this figure, we can observe that the present model gives satisfactory agreement with the prediction of the first-order slip velocity. Cavity flow at various values of *Kn* was solved since the complex geometry of cavity underneath the slider plays a critical role in determining the stability of the slider under high speed operation of the HDI system. Figure 33 shows streamlines of cavity flow. The center

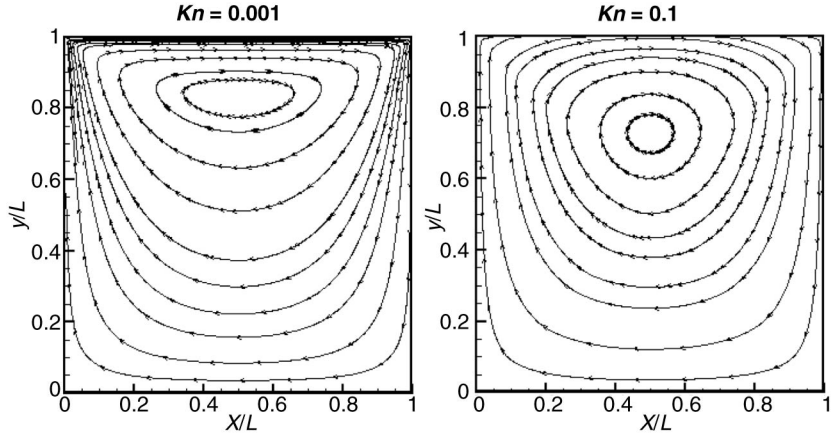

Figure 33 Streamlines of cavity flow at various Knudsen numbers.

of primary vortex moves down as Kn increases and the flow pattern was well resolved in Figure 33.

In fact, for the transition flow regime ($0.1 < Kn < 10$) and free molecular regime ($Kn > 10$), it is extremely difficult to accurately predict the flow physics using the LBM because LBM's finite discrete velocities cannot simulate the real molecule motion at high Kn. As a remedy to this problem, virtual wall collision (VWC) method has been developed (Toschi and Succi, 2005) and it was reported that LBM with VWC can solve the flow regime ($Kn < 30$). This is capable of simulating the nanoscale air bearing flow using LBM. By incorporating the SRS model introduced in Section 4.2, the entire HDI can be described by LBM providing the framework for a tribological study of the disk surface, lubricant, and read/write head. Optimization strategies can be devised by macrosopic observables from the integrated HDI model with respect to the fundamental molecular architectures, and will allow for efficient evaluation of the decision variables enabling inverse optimization formulation (Figure 15).

7. SUMMARY AND CONCLUSIONS

A holistic strategy in hierarchical modeling, which enables the communication between physical phenomena in different length and time scales and provides understanding of the systematic properties using nanoscale parameters has been presented in this paper via two benchmark systems, that is, HDD and PEFC. By illustrating representative modeling methods on each level of scale, physical phenomena in each

subsystem have been examined and the possibilities of integrating different scale methods were provided. As detailed in the benchmark systems separately, bridging methodologies enabling a link to the subsystems organically were discussed as a key to build the successful multi-scale model. Bridging the molecular to the continuum scales can be resolved via LBM in a broad range of scales from meso-scale to continuum levels. Molecular-level models with quantum level parameters can be incorporated to LBM via coarse-graining procedure, which simplify detailed molecular structures while transferring essential physics to upper scale level. The parameters in highly coarse-grained SRS model include nanoscopic information stochastically obtained from sequential coarse graining procedures including *ab initio* and bead-spring model.

As reviewed in this paper, multi-scale modeling currently is an active area with many multi-scale integration methods recently published. Although these advances in modeling techniques and multi-scale approaches for each application bring profound understanding of complex systems and provide multidisciplinary impact in multiple science and engineering fields, critical challenges are yet to be overcome in obtaining feasible methodologies. Current state of the bridging methods for the specific systems must be improved to establish a sound theoretical structure of hierarchical multi-scale integration for feasible methods. In particular, the supplemental integration methodologies between molecular and continuum scales are a major hurdle to be resolved first. In addition to the integration of time and length scales differences, the multiphenomenological integration in an identical space–time phase (e.g., heat and mass transfer and reaction kinetics) should be incorporated. For instance, the thermal effects on the nanoscale systems can be described more accurately by LBM due to its treatment of broad length and time scales. Electrons as well as phonons play a vital role in the energy transport in the nanoscale systems, therefore a thermal behavior of both electrons and phonons needs to be simultaneously considered to predict the transient sub-continuum thermal transport. LBM can also successfully accommodate for such complicated systematic problems since the complexity of the collision term in the BTE can be significantly reduced by using the single relaxation time approximation (Ghai *et al.*, 2005, 2006a, 2006b).

The demand for the research will cover the development of the novel algorithms utilizing parallel computation methods. The development of a hierarchical multi-scale paradigm will consolidate theoretical analysis and will lead to large-scale decision-making criteria of the process level design based on the first-principle dynamics.

ACKNOWLEDGMENT

One of the authors (MSJ) was supported by Korea Science & Engineering Foundation through the WCU Project.

REFERENCES

Allen, M. P. and Tildesley, D. J., ''Computer Simulation of Liquids''. Oxford, Clarendon (1996).
Baeurle, S. A., *J. Math. Chem.* **46**, 363 (2009).
Baxter, S. F., Battaglia, V. S. and White, R. E., *J. Electrochem. Soc.* **146**, 437 (1999).
Bent, J., Hutchings, L. R., Richards, R. W., Gough, T., Sparez, R., Coates, P. D., Grillo, I., Harlen, O. G., Read, D. J., Graham, R. S., Likhtman, A. E., Groves, D. J., Nicholson, T. M. and McLeish, T. C. B., *Science* **301**, 1691 (2003).
Beskok, A., *Num. Heat Trans.: Fundam.* **40**, 451 (2001).
Biegler, L. T., Grossman, I. E. and Westerberg, A. W., ''Systematic Methods of Chemical Process Design''. Prentice-Hall, Upper Saddle River, NJ (1997).
Broughton, J. Q., Abraham, F. F., Bernstein, N. and Kaxiras, E., *Phys. Rev. B* **60**, 2391 (1999).
Brown, A. E. X., Litvinov, R. I., Discher, D. E., Purohit, P. K. and Weisel, J. W., *Science* **325**, 741 (2009).
Cancelliere, A., Chang, C., Foti, E., Rothman, D. H. and Succi, S., *Phys. Fluids A* **2**, 2085 (1990).
Chen, S. and Doolen, G. D., *Annu. Rev. Fluid Mech.* **30**, 329 (1998).
Choe, Y. K., Tsuchida, E., Ikeshoji, T., Ohira, A. and Kidena, K. J., *Phys. Chem. B* **114**, 2411 (2010).
Chung, P. S., Park, H. and Jhon, M. S., *IEEE Trans. Magn.* **45**, 3644 (2009).
Coffey, T. and Krim, J., *Phys. Rev. Lett.* **96**, 186104 (2006).
Csanyi, G., Albaret, T., Payne, M. C. and De Vita, A., *Phys. Rev. Lett.* **93**, 75503 (2004).
Dalton, L. R., *Thin Solid Films* **518**, 428 (2009).
Dalton, L. R., Sullivan, P. A., Bale, D. H. and Olbricht, B. C., *Solid State Electron.* **51**, 1263 (2007).
Delgado-Buscalioni, R. and Coveney, P. V., *Phys. Rev. E* **67**, 46704 (2003).
Delle Site, L., Abrams, C. F., Alavi, A. and Kremer, K., *Phys. Rev. Lett.* **89**, 56103 (2002).
Delle Site, L. and Kremer, K., *J. Q. Chem. Int.* **101**, 733 (2005).
Delle Site, L., Leon, S. and Kremer, K. J., *Am. Chem. Soc.* **126**, 2944 (2004).
Dienwiebel, M., Verhoeven, G. S., Pradeep, N., Frenken, J. W. M., Heimberg, J. A. and Zandbergen, H. W., *Phys. Rev. Lett.* **92**(12), 126101 (2004).
Dohle, H., Divisek, J. and Jung, R. J., *Power Sources* **86**, 469 (2000).
Doi, M., *Macromol. Symp.* **195**, 101 (2003).
Dudukovic, M. P., *Science* **325**, 698 (2009).
Engler, A. J., Humbert, P. O., Wehrle-Haller, B. and Weaver, V. M., *Science* **324**, 208 (2009).
Ergun, S., *Chem. Eng. Prog.* **48**, 89 (1952).
Evans, D. J. and Morriss, G. P., *Phys. Rev. A* **30**, 1528 (1984).
Evans, D. J. and Morriss, G. P., ''Statistical Mechanics of Nonequilibrium Liquids''. Academic Press, London (1990).
Falk, M., *Can. J. Chem.* **58**, 1495 (1980).
Faller, R., *Polymer* **45**, 3869 (2004).
Flekkoy, E. G., Wagner, G. and Feder, J., *Europhys. Lett.* **52**, 271 (2000).
Franco, A. A. and Gerard, M. J., *Electrochem. Soc.* **154**, B712 (2007).
Franco, A. A. and Gerard, M. J., *Electrochem. Soc.* **155**, B367 (2008).

Franco, A. A., Passot, S., Fugier, P., Anglade, C., Billy, E., Guetaz, L., Guillet, N., Vito, E. D. and Mailley, S. J., *Electrochem. Soc.* **156**, B410 (2009).
Frenkel, D. and Smit, B., ''Understanding Molecular Simulation''. Academic Press, New York (2000).
Frenklach, M., Packard, A., and Seiler, P. (2002). American Control Conference, Anchorage, May 8–10, pp. 4135–4140.
Frenklach, M., Packard, A., Seiler, P. and Feeley, R., *Int. J. Chem. Kinet.* **36**, 57 (2004).
Fukui, S. and Kaneko, R., *JSME Int. J.* **30**, 1660 (1987).
Fung, M. K., Lai, K. H., Lai, H. L., Chan, C. Y., Wong, N. B., Bello, I., Lee, C. S. and Lee, S. T., *Diamond Relat. Mater.* **9**, 815 (2000).
Gerde, E. G. and Marder, M., *Nature* **413**, 286 (2001).
Ghai, S. S., Chung, P. S., Kim, W. T., Amon, C. H. and Jhon, M. S., *IEEE Trans. Magn.* **42**, 2474 (2006).
Ghai, S. S., Kim, W. T., Escobar, R. A., Amon, C. H. and Jhon, M. S., *J. Appl. Phys.* **97**, 10P703 (2005).
Ghai, S. S., Kim, W. T., Amon, C. H. and Jhon, M. S., *J. Appl. Phys.* **99**, 08F906 (2006).
Gierke, T. D., Munn, G. E. and Wilson, F. C., *J. Polym. Sci.* **19**(Part A-2), 1687 (1981).
Glotzer, S. C. and Paul, W., *Annu. Rev. Mater. Res.* **32**, 401 (2002).
Goddard III, W., Merinov, B., Van Duin, A., Jacon, T., Blanco, M., Molinero, V., Jang, S. S. and Jang, Y. H., *Mol. Simulat.* **32**, 251 (2006).
Gorban, A. N., Kazantzis, N., Kevrekidis, I. G., Ottinger, H. C. and Theodoropoulos, K., ''Model Reduction and Coarse-Graining Approaches for Multiscale Phenomena''. Springer, New York (2006).
Grest, G. S. J., *Chem. Phys.* **105**, 5532 (1996).
Grossmann, I. E. and Westerberg, A. W., *AIChE J.* **46**, 1700 (2000).
Gubbins, K. E. and Moore, J. D., *Ind. Eng. Chem. Res.* **49**, 3026 (2010).
Guerra, R., Tartaglino, U., Vanossi, A. and Tosatti, E., *Nat. Mater.* **9**, 634 (2010).
Guo, Q., Chen, H. G., Smith, B. C. and Jhon, M. S., *J. Appl. Phys.* **97**, 10P301 (2005).
Guo, Q., Chung, P. S., Chen, H. G. and Jhon, M. S., *J. Appl. Phys.* **99**, 08N105 (2006).
Guo, Q., Izumisawa, S., Jhon, M. S. and Hsia, Y. T., *IEEE Trans. Magn.* **40**, 3177 (2004).
Guo, Q., Izumisawa, S., Phillips, D. M. and Jhon, M. S., *J. Appl. Phys.* **93**, 8707 (2003).
Guo, Z. L. and Zhao, T. S., *Phys. Rev. E* **66**, 036304 (2002).
Habenicht, B. F., Paddison, S. J. and Tuckerman, M. E., *J. Mater. Chem.* **20**, 6342 (2010).
Hadjiconstantinou, N. G., *Phys. Rev. E* **59**, 2475 (1999).
Hao, L. and Cheng, P J., *Power Sources* **195**, 3870 (2010).
Haubold, H. G., Vad, T., Jungbluth, H. and Hiller, P., *Electrochim. Acta* **46**, 1559 (2001).
Hijón, C., Español, P., Vanden-Eijnden, E. and Delgado-Buscalioni, R., *Faraday Discuss.* **144**, 285 (2010).
Hohenberg, P. and Kohn, W., *Phys. Rev.* **136**, B864 (1964).
Hoover, W. G., Evans, D. J., Hickman, R. B., Ladd, A. J. C., Ashurst, W. T. and Moran, B., *Phys. Rev. A* **22**, 1690 (1980).
Hsia, Y. T. and Domoto, G. A., *ASME. J. Lub. Tech.* **105**, 120 (1983).
Ilg, P., Öttinger, H. C. and Kröger, M., *Phys. Rev. E* **79**, 011802 (2009).
Iuchi, S., Izvekov, S. and Voth, G. A., *J. Chem. Phys.* **126**, 124505 (2007).
Izumisawa, S. and Jhon, M. S., *J. Chem. Phys.* **117**, 3972 (2002).
Izumisawa, S. and Jhon, M. S., *Tribol. Lett.* **12**, 75 (2002).
Izvekov, S., Violi, A. and Voth, G. A., *J. Phys. Chem. B* **109**, 17019 (2005).
Izvekov, S. and Voth, G. A., *J. Phys. Chem. B* **109**, 2469 (2005).
Izvekov, S. and Voth, G. A., *J. Phys. Chem.* **123**, 134105 (2005).
Izvekov, S. and Voth, G. A., *J. Chem. Phys.* **125**, 151101 (2006).
Izvekov, S. and Voth, G. A., *J. Chem. Theory Comput.* **2**, 637 (2006).
Jain, P., Biegler, L. T. and Jhon, M. S., *J. Electrochem. Soc.* **157**, B1222 (2010).

Jain, P., Jhon, M. S. and Biegler, L. T., *Electrochem. Solid. St.* **11**, B193 (2008).
Jensen, F., ''Introduction to Computational Chemistry''. Wiley, Chichester (1999).
Jhon, M. S. and Choi, H. J., *J. Ind. Eng. Chem.* **7**, 263 (2001).
Jhon, M. S., Izumisawa, S., Guo, Q., Phillips, D. M. and Hsia, Y. T., *IEEE Trans. Magn.* **39**, 754 (2003).
Jhon, M. S., Smith, R., Vemuri, S. H., Chung, P. S., Kim, D. and Biegler, L. T., *IEEE Trans. Magn.* **47**, 87 (2011).
Jinnouchi, R. and Okazaki, K. J., *Electrochem Soc.* **150**, E66 (2003).
Johnson, E. R. and DiLabio, G. A., *Phys. Lett.* **419**, 333 (2006).
Johnson, E. R., Mackie, L. D. and DiLabio, G. A., *J. Phys. Org. Chem.* **22**, 1127 (2009).
Johnson, K. E., Mate, C. M., Merz, J. A., White, R. L. and Wu, A. W., *IBM J. Res. Dev.* **40**(5), 511 (1996).
Juan, M. L., Plain, J., Bachelot, R., Royer, P., Gray, S. K. and Wiederrecht, G. P., *ACS Nano* **3**, 1573 (2009).
Kang, S. -C., Crone, R. M. and Jhon, M. S., *J. Appl. Phys.* **85**, 5594 (1999).
Karis, T. E., Kim, W. T. and Jhon, M. S., *Tribol. Lett.* **18**, 27 (2005).
Karis, T. E., Marchon, B., Flores, V. and Scarpulla, M., *Tribol. Lett.* **11**, 151 (2001).
Kasai, P. H., *Tribol. Lett.* **13**, 155 (2002).
Kasai, P. H. and Spool, A. M., *IEEE Trans. Magn.* **37**, 929 (2001).
Kasai, P. H., Wass, A. and Yen, B. K., *J. Inf. Stor. Proc. Syst.* **1**, 245 (1999).
Kim, W. T., Ghai, S. S., Zhou, Y., Staroselsky, I., Chen, H. D. and Jhon, M. S., *IEEE Trans. Magn.* **41**(10), 3016 (2005).
Kim, W. T., Jhon, M. S., Zhou, Y., Staroselsky, I. and Chen, H. J., *Appl. Phys.* **97**(10), 10P304 (2005).
Kim, H. M., Kim, D., Kim, W. T., Chung, P. S. and Jhon, M. S., *IEEE Trans. Magn.* **43**, 2244 (2007).
Kim, T. -D., Lao, J., Cheng, Y. -J., Shi, Z., Hau, S., Jang, S. -H., Zhou, X. -H., Tian, Y., Polishak, B., Huang, S., Ma, H., Dalton, L. R. and Jen, A. K. -Y. J., *Phys. Chem. C* **112** (21), 8091 (2008).
Klaus, E. and Bhushan, B., *Tribol. Mech. Magn. Storage Syst.* **SP-19**, 7 (1985).
Kohn, W., Meir, Y. and Makarov, D. E., *Phys. Rev. Lett.* **80**, 4153 (1998).
Komarov, P. V., Veselov, I. N., Chu, P. P., Khalatur, P. G. and Khokhlov, A. R., *Chem. Phys. Lett.* **487**, 291 (2010).
Krishnan, M., Verma, A. and Balasubramanian, S., *Proc. Indian Acad. Sci. (Chem. Sci.)* **113**, 579 (2001).
Laio, A., VandeVondele, J. and Röthlisberger, U. J., *Chem. Phys.* **116**, 6941 (2002).
Lang, Y.-D., Biegler, L. T., and Zitney, S. E. (2011). *Comput. Chem. Eng.*, doi:10.1016/j.compchemeng.2011.01.018.
Lang, Y-D., Malacina, A., Biegler, L. T., Munteanu, S., Madsen, J. I. and Zitney, S. E., *Energ. Fuel.* **23**, 1695 (2009).
Leconte, N., Moser, J., Ordejon, P., Tao, H., Lherbier, A., Bachtold, A., Alsina, F., Sotomayor Torres, C. M., Charlier, J. -C. and Roche, S., *ACS Nano* **4**, 4033 (2010).
Lee, H., Lee, N., Seo, Y., Eom, J. and Lee, S., *Nanotechnology* **20**, 325701 (2009).
Lee, C., Li, Q., Kalb, W., Liu, X. -Z., Berger, H., Carpick, R. W. and Hone, J., *Science* **328**, 76 (2010).
Lee, J. K., Smallen, M., Enguero, J., Lee, H. J. and Chao, A., *IEEE Trans. Magn.* **29**, 276 (1993).
Lee, T. D. and Yang, C. N., *Phys. Rev.* **87**, 410 (1952).
Lemke, J. U., French, W. W., and McHargue, W. B. (1994). U.S. Patent 5317463.
LeSar, R. J., *Phys. Chem* **88**, 4272 (1984).
Li, J., Liao, D. and Yip, S., *Phys. Rev. E* **57**, 7259 (1998).
Lucas, M., Zhang, X., Palaci, I., Klinke, C., Tosatti, E. and Riedo, E., *Nat. Mater.* **8**, 876 (2009).
Lyubartsev, A. P. and Laaksonen, A., *Phys. Rev. E* **52**, 3730 (1995).

Ma, X., Bauer, C. L., Jhon, M. S., Gui, J. and Marchon, B., *Phys. Rev. E* **60**, 5795 (1999).
Ma, X., Gui, J., Grannen, K., Smoliar, L., Marchon, B., Jhon, M. S. and Bauer, C. L., *Tribol. Lett.* **6**, 9 (1999).
Ma, X., Gui, J., Smoliar, L., Grannen, K., Marchon, B., Bauer, C. L. and Jhon, M. S., *Phys. Rev. E* **59**(1), 722 (1999).
Ma, X., Gui, J., Smoliar, L., Grannen, K., Marchon, B., Jhon, M. S. and Bauer, C. L., *J. Chem. Phys.* **110**, 3129 (1999).
Maginn, E. J. and Elliot, J. R., *Ind. Eng. Chem. Res.* **49**, 3059 (2010).
Marchon, B., Guo, X. C., Karis, T., Deng, H., Dai, Q., Burns, J. and Waltman, R. J., *IEEE Trans. Magn.* **42**(10), 2504 (2006).
Marquardt, W., Von Wedel, L. and Bayer, B., *AIChE Sym. Ser.* **96**(323), 192 (2000).
McGreevy, R. L., *Nucl. Instrum. Meth. A* **1**, 354 (1995).
McGreevy, R. L. and Pusztai, L., *Mol. Simul.* **1**, 359 (1988).
Mei, R., Shyy, W., Yu, D. and Luo, L. J., *Comp. Phys.* **161**, 680 (2000).
Meijer, E. J. and Sprik, M. J., *Chem. Phys.* **105**, 8684 (1996).
Mench, M. M., Wang, C. Y. and Thynell, S. J., *Electrochem. Soc.* **151**, A144 (2004).
Metropolis, N., Rosenbluth, A. W., Rosenbluth, M. N., Teller, A. H. and Teller, E. J., *Chem. Phys.* **21**, 1087 (1953).
Milchev, A. and Binder, K., *Macromolecules* **29**, 343 (1996).
Milchev, A., Paul, W. and Binder, K. J., *Chem. Phys.* **99**, 4786 (1993).
Miura, K., Kamiya, S. and Sakai, N., *Phys. Rev. Lett.* **90**(5), 055509-1 (2003).
Moseler, M., Gumbsch, P., Casiraghi, C., Ferrari, A. C. and Robertson, J., *Science* **309**, 1545 (2005).
Mukherjee, P. P. and Wang, C. Y., *J. Electrochem. Soc.* **153**, A840 (2006).
Mukherjee, P. P. and Wang, C. Y., *J. Electrochem. Soc.* **154**, B1121 (2007).
Myong, R. S., Reese, J. M., Barber, R. W. and Emerson, D. R., *Phys. Fluids* **17**, 087105 (2005).
Neri, M., Anselmi, C., Cascella, M., Maritan, A. and Carloni, P., *Phys. Rev. Lett.* **95**, 218102 (2005).
Nithiarasu, P., Seetharamu, K. N. and Sundararajan, T., *Int. J. Heat Mass Trans.* **40**, 3955 (1997).
Noid, W. G., Chu, J. W., Ayton, G. S., Krishna, V., Izvekov, S., Voth, G. A., Das, A. and Andersen, H. C., *J. Chem. Phys.* **128**, 244114 (2008).
Noid, W. G., Liu, P., Wang, Y., Chu, J. W., Ayton, G. S., Izvekov, S., Andersen, H. C. and Voth, G. A., *J. Chem. Phys.* **128**, 244115 (2008).
Oberkampf, W. L., Trucano, T. G., and Hirsch, C. (2002). Proc. Foundations 02, Johns Hopkins University, Laurel, MD, October.
O'Connell, S. T. and Thompson, P. A., *Phys. Rev. E* **52**, R5792 (1995).
O'Connor, T. M., Back, Y. R., Jhon, M. S., Min, B. G. and Karis, T. E., *J. Appl. Phys.* **79**, 5788 (1996).
Olbricht, B. C., Sullivan, P. A., Wen, G. -A., Misty, A., Davies, J. A., Ewy, T. R., Eichinger, B. E., Robinson, B. H., Reid, P. J. and Dalton, L. R., *J. Phys. Chem. C* **112**(21), 7983 (2008).
Parr, R. G. and Yang, W., ''Density-Functional Theory of Atoms and Molecules''. Oxford University, New York (1989).
Pearson, J. D., Gao, G., Zikry, M. A. and Harrison, J. A., *Comput. Mater. Sci.* **47**, 1 (2009).
Pereverzev, Y. V., Gunnerson, K. N., Prezhdo, O. V., Sullivan, P. A., Liao, Y., Olbricht, B. C., Akelaitis, A. J. P., Jen, A. K. -Y. and Dalton, L. R., *J. Phys. Chem. C* **112**, 4355 (2008).
Phillips, D. M. and Jhon, M. S., *J. Appl. Phys.* **91**, 7577 (2002).
Phillips, D. M., Khair, A. S. and Jhon, M. S., *IEEE Trans. Magn.* **37**, 1866 (2001).
Pit, R., Marchon, B., Meeks, S. and Velidandla, V., *Tribol. Lett.* **10**, 133 (2001).
Porat, Z., Fryer, J. R., Huxham, M. and Rubinstein, I. J., *Phys. Chem.* **99**, 4667 (1995).
Rafii-Tabar, H., Hua, L. and Cross, M. J., *Phys. Condens. Matter* **10**, 2375 (1998).

Rama, P., Liu, Y., Chen, R., Ostadi, H., Jiang, K., Gao, Y., Zhang, X., Fisher, R. and Jeschke, M., *Energy Fuel* **24**, 3130 (2010).
Reith, D., Putz, M. and Müller-Plathe, F., *J. Comput. Chem.* **24**, 1624 (2003).
Ren, X. M., Springer, T. E. and Zawodzinski, T. A., *J. Electrochem. Soc.* **147**, 466 (2000).
Roche, E. J., Pineri, M., Duplessix, R. and Levelut, A. M., *J. Polym. Sci. Polym. Phys. Ed.* **19**, 1 (1981).
Rubla, T. D., Zblb, H. M., Khralshl, T. A., Wirth, B. D., Victoria, M. and Caturla, M. J., *Nature* **406**, 871 (2000).
Sakane, Y., Wakabayashi, A., Li, L. and Kasai, P. H., *IEEE Trans. Magn.* **42**(10), 2501 (2006).
Sbragaglia, M. and Succi, S., *Phys. Fluids* **17**, 093602 (2005).
Schirmeisen, A., *Nat. Mater.* **9**, 615 (2010).
Seminario, J. M., *Int. J. Q. Chem.* **60**, 1271 (1996).
Sheng, Y. J., Panagiotopoulos, A. Z., Kumar, S. K. and Szleifer, I., *Macromolecules* **27**, 400 (1994).
Shi, Q., Izvekov, S. and Voth, G. A., *J. Phys. Chem. B* **110**, 15045 (2006).
Smirnova, J. A., Zhigilei, L. V. and Garrison, B. J., *Comput. Phys. Commun.* **118**, 11 (1999).
Smith, R., Chung, P. S., Steckel, J. A., Jhon, M. S. and Biegler, L. T., *J. Appl. Phys.* **109**, 07B728 (2011).
Soper, A. K., *Chem. Phys.* **202**, 295 (1996).
Sukop, M. C., Huang, H., Lin, C. L., Deo, M. D., Oh, K. and Miller, J. D., *Phys. Rev. E* **77**, 026710 (2008).
Sullivan, P. A., Rommel, H., Liao, Y., Olbricht, B. C., Akelaitis, A. J. P., Firestone, K. A., Kang, J. -W., Luo, J., Choi, D. H., Eichinger, B. E., Reid, P. J., Chen, A., Jen, A. K. Y., Robinson, B. H. and Dalton, L. R., *J. Am. Chem. Soc.* **129**, 7523 (2007).
Tani, H. and Matsumoto, H., *Tribol. Int.* **36**, 397 (2003).
Theodorou, D. N., *Comput. Phys. Commun.* **169**, 82 (2005).
Theodorou, D. N., *Ind. Eng. Chem. Res.* **49**, 3047 (2010).
Toschi, F. and Succi, S., *Europhys. Lett.* **69**, 549 (2005).
Tyndall, G. W., Karis, T. E. and Jhon, M. S., *Tribol. Trans.* **42**, 463 (1999).
Ulherr, A. and Theodorou, D. N., *Curr. Opin. Solid State Mater. Sci.* **3**, 544 (1998).
Vafai, K., *J. Fluid Mech.* **147**, 233 (1984).
Villa, E., Balaeff, A., Mahadevan, L. and Schulten, K., *Multiscale Model. Simul.* **2**, 527 (2004).
Vinay, S. J., Phillips, D. M., Lee, Y. S., Schroeder, C. M., Ma, X. D., Kim, M. C. and Jhon, M. S., *J. Appl. Phys.* **87**, 6164 (2000).
Vlachos, D. G., *Adv. Chem. Eng.* **30**, 1 (2005).
Waltman, R. J., Khurshudov, A. and Tyndall, G. W., *Tribol. Lett.* **12**, 163 (2002).
Waltman, R. J., Pocker, D. and Tyndall, G. W., *Tribol. Lett.* **4**, 267 (1998).
Waltman, R. J., Tyndall, G. W. and Pacansky, J., *Langmuir* **15**, 6470 (1999).
Waltman, R. J., Tyndall, G. W., Pacansky, J. and Berry, R. J., *Tribol. Lett.* **7**, 91 (1999).
Wang, Y. T., Izvekov, S., Yan, T. Y. and Voth, G. A., *J. Phys. Chem. B* **110**, 3564 (2006).
Wang, G., Mukherjee, P. P. and Wang, C. Y., *Electrochim. Acta* **51**, 3139 (2006).
Wang, G., Mukherjee, P. P. and Wang, C. Y., *Electrochim. Acta* **51**, 3151 (2006).
Wang, G., Mukherjee, P. P. and Wang, C. Y., *Electrochim. Acta* **52**, 6367 (2007).
White, R. T., Bhatia, S. S., Friedenberg, M. C., Meeks, S. W., and Mate, C. M. (1996). Tribology of Contact/Near Contact Recording for Ultra High Density Magnetic Storage, ASME/STLE Tribology Conference, San Francisco, CA.
Xu, C., Biegler, L. T. and Jhon, M. S., *AIChE J.* **52**, 2496 (2006).
Xu, Y. S., Liu, Y., Zu, X. Z. and Huang, G. X., *J. Electrochem. Soc.* **153**, A607 (2006).
Yu, Z. and Fan, L. S., *Phys. Rev. E* **82**, 046708 (2010).
Zhou, J., Thorpe, I. F., Izvekov, S. and Voth, G. A., *Biophys. J.* **92**, 4289 (2007).
Zhu, L., Zhang, J., Liew, T. and Ye, K. D., *J. Vac. Sci. Technol. A* **21**, 1087 (2003).